RESEARCH ARTICLE

Zircon Dates Long-Lived Plume Dynamics in Oceanic Islands

Yamirka Rojas-Agramonte[1,2,3] , Boris J. P. Kaus[3] , Andrea Piccolo[3,4] , Ian S. Williams[5] , Axel Gerdes[6,7], Jean Wong[8], HangXian Xie[2] , Stephan Buhre[3], Theofilos Toulkeridis[9], Pilar Montero[10], and Antonio Garcia-Casco[10,11]

[1]Institut für Geowissenschaften, Christian-Albrechts-Universität zu Kiel, Kiel, Germany, [2]Beijing SHRIMP Centre, Chinese Academy of Geological Sciences, Beijing, China, [3]Institute of Geosciences, University of Mainz, Mainz, Germany, [4]Bayerisches Geoinstitut, Universität Bayreuth, Bayreuth, Germany, [5]Research School of Earth Sciences, Australian National University, Canberra, ACT, Australia, [6]Department of Geosciences, Goethe-University Frankfurt, Frankfurt, Germany, [7]Frankfurt Isotope and Element Research Center (FIERCE), Goethe-University Frankfurt, Frankfurt, Germany, [8]Department of Earth Sciences, The University of Hong Kong, Beijing, China, [9]Universidad de las Fuerzas Armadas ESPE, Sangolquí, Ecuador, [10]Department of Mineralogy and Petrology, University of Granada, Granada, Spain, [11]Andalusian Earth Sciences Institute (IACT), University of Granada-CSIC, Granada, Spain

Abstract In this contribution we report the first systematic study of zircon U-Pb geochronology and $\delta^{18}O$-$\varepsilon Hf_{(t)}$ isotope geochemistry from 10 islands of the hot-spot related Galapagos Archipelago. The data extracted from the zircons allow them to be grouped into three types: (a) young zircons (0–~4 Ma) with $\varepsilon Hf_{(t)}$ (~5–13) and $\delta^{18}O$ (~4–7) isotopic mantle signature with crystallization ages dating the islands, (b) zircons with $\varepsilon Hf_{(t)}$ (~5–13) and $\delta^{18}O$ (~5–7) isotopic mantle signature (~4–164 Ma) which are interpreted to date the time of plume activity below the islands (~164 Ma is the minimum time of impingement of the plume below the lithosphere), and (c) very old zircons (~213–3,000 Ma) with mostly continental (but also juvenile) $\varepsilon Hf_{(t)}$ (~−28–8) and $\delta^{18}O$ (~5–11) isotopic values documenting potential contamination from a number of sources. The first two types with similar isotopic mantle signature define what we call the Galápagos Plume Array (GPA). Given lithospheric plate motion, this result implies that GPA zircon predating the Galápagos lithosphere (i.e., >14–164 Ma) formed and were stored at sublithospheric depths for extended periods of time. In order to explain these observations, we performed 2D and 3D thermo-mechanical numerical experiments of plume-lithosphere interaction which show that dynamic plume activity gives rise to complex asthenospheric flow patterns and results in distinct long-lasting mantle domains beneath a moving lithosphere. This demonstrates that it is physically plausible that old plume-derived zircons survive at asthenospheric depths below ocean islands.

1. Introduction and Geological Setting

Global tomography and numerical models suggest that mantle plume occurrences are closely linked to the margins of large low-shear velocity provinces (Burke et al., 2008; French & Romanowicz, 2015; Garnero et al., 2016; Torsvik et al., 2014). In these marginal zones, the ascent of material connects deep mantle dynamics with surface processes through prolonged mantle plume activity. This will eventually form large igneous provinces (LIPs), hotspot tracks and volcanoes (Steinberger & Torsvik, 2012), like the modern Galápagos Archipelago (Figure 1), Hawai'i and Easter Islands. Recent studies suggest that despite striking differences in the surficial expression of the Galápagos, Eastern and Hawai'i plumes, they share a common generation mechanism originating at the Pacific LLSVP (Harpp, 2020; Harpp et al., 2014). The onset of hotspot magmatism is often marked by a LIP, a term including continental flood basalts and oceanic plateaus. LIPs are usually considered the result of short-lived (~1–2 Ma) periods of intense volcanism after the impingement of mantle plumes at the base of the oceanic or the continental lithosphere (Kerr & Mahoney, 2007; Sobolev et al., 2011). LIPs have also been associated with episodes of anoxia and mass extinction shortly after their eruption. In addition, they are associated with some of the largest ore deposits in the world (e.g., Ni-Cu-PGE, Fe-Ti-V, and Cr ore depositsErnst & Jowitt, 2013).

Mantle plumes are active for long periods (Madrigal et al., 2016), however constraining their evolution through time is complicated because of the difficulty in obtaining precise absolute age relationships in the mafic rocks found in this setting and the fact that, in the oceanic environment, the plume products located in the lithosphere drift away and eventually are lost upon subduction. One of the most precise geochronometers is the U-Pb in zircon ($ZrSiO_4$), but the zircon abundance in the oceanic crust is limited due to the incompatible nature of the

Piccolo, Ian S. Williams, Theofilos
Toulkeridis, Antonio Garcia-Casco
Methodology: Boris J. P. Kaus, Andrea
Piccolo, Axel Gerdes, Jean Wong,
HangXian Xie, Stephan Buhre, Pilar
Montero
Writing – original draft: Yamirka Rojas-
Agramonte, Boris J. P. Kaus, Andrea
Piccolo, Ian S. Williams, Theofilos
Toulkeridis, Antonio Garcia-Casco
Writing – review & editing: Yamirka
Rojas-Agramonte, Boris J. P. Kaus,
Antonio Garcia-Casco

element Zirconium (Zr) and the scarce abundance of Zr in basaltic magmas. Zircon forms after fractional crystallization of primitive Zr-subsaturated basaltic magmas (Davies et al., 2021; Pujol-Solà et al., 2020) and is stable down to ~300 km depths, below which it transforms into reidite (Akaogi et al., 2018). In addition, recent studies show crystallization of zircon in low-Zr mafic magmas of the mid-Atlantic ridge is possible (Bea et al., 2022) but must involve the formation of small (local) zircon-saturated transient zones near growing minerals interfaces. This opens a new window for research on the age of prolonged focused magmatic activity at sub lithospheric depths, such as in mantel plumes, with significant geodynamic implications for asthenosphere-lithosphere interactions and asthenospheric flow.

Mantle plume upwelling in the Pacific has been active since at least the mid-Jurassic, as recorded in the Pigafetta Basin, which contains the oldest oceanic crust of the Pacific plate (~170–160 Ma) (Fisk & Kelley, 2002; Seton et al., 2020). The Pacific plates offshore Central America, Colombia-Ecuador, the Caribbean and associated accreted onshore rock exposures, contain a Mesozoic to recent record of Pacific mantle upwelling events that resulted in new oceanic lithosphere, LIPs and hotspot tracks (Andjić et al., 2019). The early plume products range from early Cretaceous to the last Pacific LIP event: the Ecuadorian-Colombian-Caribbean LIP (ECCLIP) that formed mostly at ~90 Ma, with potential additional events in the range 139–74 Ma (Dürkefälden et al., 2019; Hoernle et al., 2004; Madrigal et al., 2016; Sinton et al., 1998). Mantle heterogeneities and recycled crust characterize this Cretaceous activity of the plume (Gazel et al., 2021; Trela et al., 2015). Though the ECCLIP is generally considered to be a product of the Galápagos plume, other authors however, based on paleomagnetic reconstructions, suggest that the ECCLIP originated 2,000 km east of the Galápagos hotspot, and may thus not be derived from the same mantle plume (Boschman et al., 2014). On the other hand (Shellnutt et al., 2021), goes further as to suggest that the Triassic volcanic rocks of Wrangellia of western North America (more than 3,000 km away from present-day Galápagos) were generated from a Pacific mantle plume source. Their paleogeographic constraints, thermal estimates, and geochemistry suggests that it is possible that the Galápagos hotspot generated the volcanic rocks of Wrangellia and the Caribbean plateau or, more broadly, that the eastern Pacific (Panthalassa) Ocean was a unique region where anomalously high thermal conditions either periodically or continually existed from at least ~230 Ma to the present day.

The hot-spot-related Galápagos Archipelago erupted on top of thin and young oceanic crust (~10 Ma in the northern part of the Archipelago, ~14 Ma in the southern part) (Harpp & Geist, 2018) created at the nearby Galápagos Spreading Center (GSC; Figure 1). Owing to the eastward motion of the Nazca plate the south easternmost islands (e.g., Española; Figure 2), are the oldest with K-Ar ages of ~2.8 Ma (White et al., 1993). Galápagos volcanoes are fed by a mix of plume- and MOR-asthenosphere-derived melts that provide important insights into heterogeneities of the mantle sources of ocean island volcanism (Blichert-Toft & White, 2001; Geist et al., 1988; Harpp & White, 2001). Isotopic and trace element compositions of basaltic lavas in the Galápagos Archipelago indicate melting of several distinct mantle sources that include components from recycled oceanic and continental crust materials (Blichert-Toft & White, 2001; Hoernle et al., 2000). Paleomagnetic and geochemical data record a complex interaction between the hot spot and the GSC (Detrick et al., 2002; Gibson et al., 2015; Harpp et al., 2003; Harpp & Geist, 2002). The interplay between the mantle plume and the GSC dates back to Oligocene times (~23 Ma), when the Farallon plate split into the Cocos and Nazca plates and the aseismic Cocos, Carnegie and Malpelo ridges started to form (Lonsdale, 2005; Meschede & Barckhausen, 2001). Upon drifting away from the GSC, the oldest parts of these hotspot tracks have been subducted at the Central America and Nazca subduction zones (the oldest present-day ages of ridges are ~11–14 Ma) (Christie et al., 1992; Werner et al., 1999).

In an effort to date magmatism in the Galapagos Archipelago, we conducted a zircon U–Pb geochronology study combined with Hf and O isotopic analysis of zircon grains from 10 Galápagos islands. Due to the scarcity of zircon in rock samples, we decided to sample not only igneous rocks but also detrital material derived from the igneous rocks of the islands (see below). The isotopic results from 238 zircon grains allow offering a strong argument for the age of the archipelago. However, unexpectedly they also allow insight into the long-term temporal evolution of the Galápagos plume, as many zircons are older than the age of the Galapagos lithosphere, posing fundamental questions on plume dynamics at asthenospheric depths and plume-lithosphere interactions. We therefore performed 2D and 3D thermo-mechanical geodynamic simulations to understand the fate of plume-derived zircon grains and the dynamics of the plume itself. Our geochemical and thermo-mechanical modeling results can likely be reproduced in other oceanic islands.
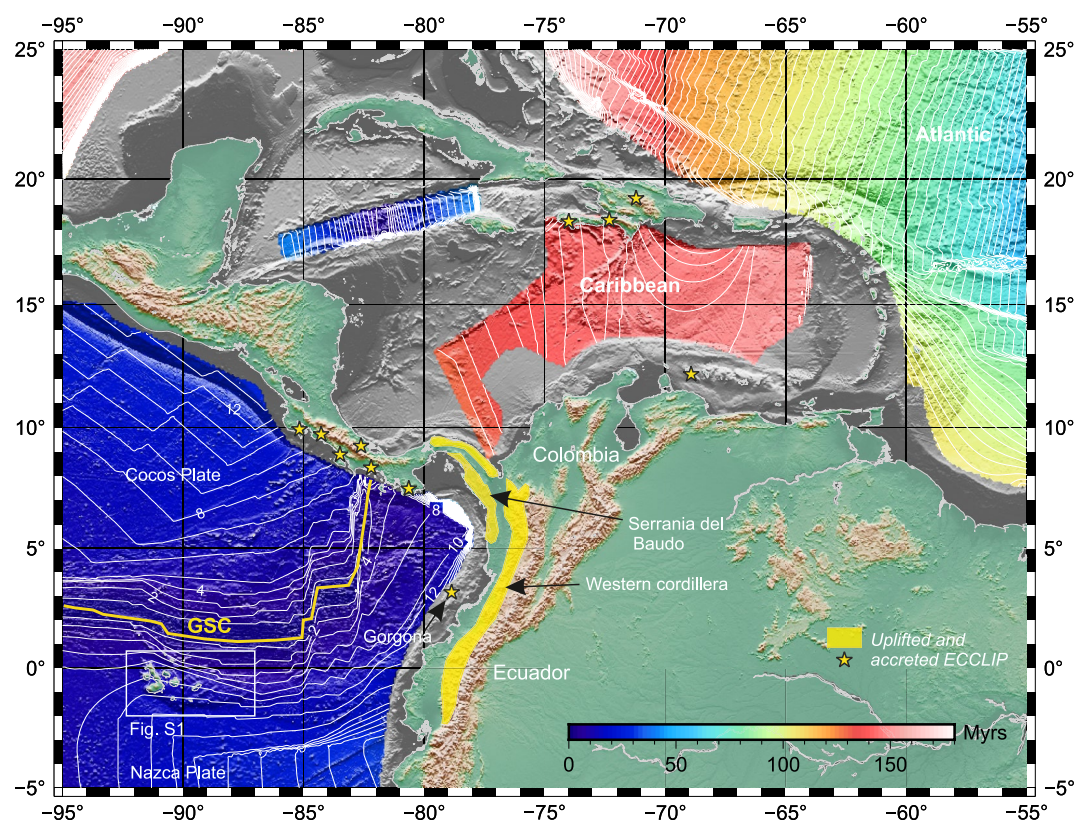
Figure 1. Plate-tectonic configuration of the Pacific and the Caribbean region and location of uplifted and accreted Ecuadorian-Colombian-Caribbean-Large-Igneous-Province (ECCLIP) fragments. See Figure 2 for sample locations containing zircon grains.

2. Methods

2.1. Sampling Strategy

We conducted an extensive sampling of basaltic and rhyolitic rocks (pumice), cave deposits collected on the floor of a lava tube and of sands from stream beds and beaches in 10 Galápagos islands (Figures 2–4; Table 1) covering most of the main area of the Archipelago. Finding rare zircons in basaltic rocks is a difficult task, therefore natural geological processes such as erosion and sediment formation are good allies in the search for zircon. Beaches and soils on oceanic islands far from the continents will have concentrates of recent material eroded from basaltic rocks that fingerprint each island (Seelos et al., 2021).

Thirty-six (36) zircon-bearing samples (Figure 2; Table 1) were retrieved from the Western (Isabela 3 samples), Central (Rábida 2, Santa Fe 5), Southern (Española 1, Floreana, 11), and Eastern (Baltra 2, Genovesa 1, Pinzón 2, San Cristobal 4, Santa Cruz 5) isotopic zones defined by Hoernle et al. (2000). From these samples we analyzed 238 zircon grains for U-Pb dating and Hf and O isotopic compositions (see Supporting Information S1 for methods and Figures 5–7).

2.2. Analytical Procedure

2.2.1. Sample Processing and Zircon Separation Approach

Sand and soil samples were collected and panned locally in beaches for heavy minerals in each island of the Galápagos Archipelago. This approach is used to reduce the risk of external and laboratory contamination to a minimum. In this way, the samples are never in contact with other samples that do not come from the island where they were taken. Similar techniques have been applied successfully in other regions of the world, for example, Mauritius (Torsvik et al., 2013), Indonesia (Sevastjanova et al., 2011), and Grenada (Rojas-Agramonte

Figure 2. Galápagos Archipelago map showing sample locations in the islands containing zircon grains and present position of the plume (Villagómez et al., 2014). (a) Beach sand sample GAL38 at Pinzón, was collected at the same location as sample GAL36. Samples that contain zircon grains older than 14 Ma are designated in bold letters and underlined (see Tables 2 and 3).
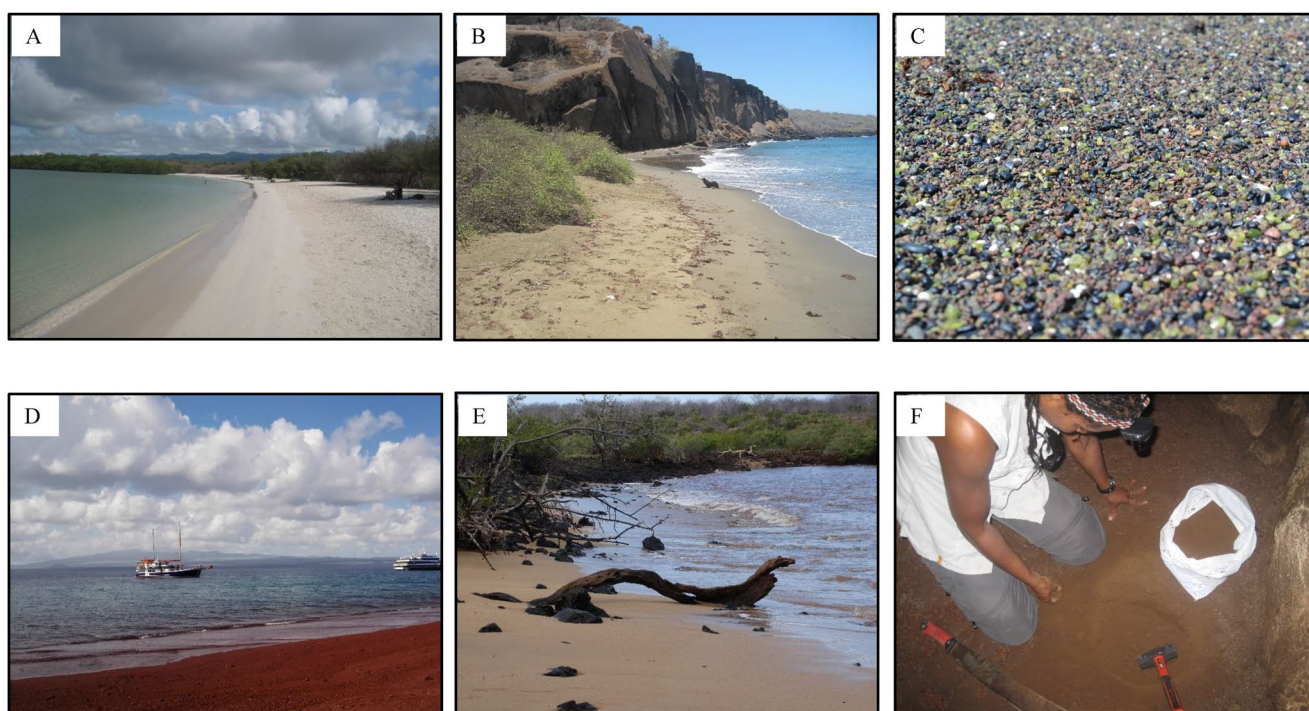
Figure 3. Examples of contrasting Galápagos beach sands (a, b, c, d, e) and a lava tube deposit (f). See Table 1 for sample/beach coordinates. (a) White sand beach from Playa Mansa at Tortuga Bay, south of Santa Cruz (GAL3), (b) Green beach (Pirate cave), northeast of Floreana (FL8, GAL149), (c) olivine beach north of Floreana. Coarse (rounded) grained beach, containing mostly mafic minerals (note green olivine) with a grain size of up to 3 mm. (d) Red beach north of Rábida, containing many young zircon grains (GAL28). (e) Las Bachas beach near canal de Itabaca, north of Santa Cruz (GAL17). (f) Soil sample (GAL6) collected at Cascajo Cave, a lava tube located in south-central Santa Cruz.

et al., 2017). The sands on beaches in Galápagos vary in composition, color and grain size as a result of biological activity and the nature of dynamic processes that affected the source rocks they come from (providing mostly grains of olivine, pyroxene and magnetite) as well as by coastal processes that modify the sand over long periods of time (Seelos et al., 2021) (Figure 3). In addition, coral reefs located offshore and the carbonate parts of other animals largely contribute to the composition of beach sands (Seelos et al., 2021).

The basalt and pumice samples were processed at Mainz University. We are aware that contamination may occur in the lab during sample preparation, therefore we took good care during the process. One of the methodologies that we use to avoid sample laboratory contamination is to "contaminate" the jaw crusher at Mainz University with glass bottles which were passed through the machine a minimum of three times before starting the preparation of the samples. Another measure we took was that work by others was not allowed in the sample separation room until the full set of Galapagos samples was finished. Approximately 1–5 kg of each whole-rock sample was crushed to a grain size of ∼250 μm, using a jaw crusher and roller mill. A first concentrate of heavy mineral fraction was then produced by panning with water and a Frantz magnetic separator at Mainz University. The final heavy mineral concentrates (mostly zircon) from rocks and detritus were obtained by panning with alcohol in the Beijing SHRIMP Centre, China. We employed the panning technique to exclude that any zircon in the mineral concentrate was due to laboratory contamination. Zircons for isotopic analysis were then handpicked during optical inspection under a binocular microscope and mounted in epoxy resin. About 100 g of the homogenized coarse rock material were powderized in a Siebtechnik® tungsten carbide mill for chemical and whole-rock isotopic analysis.

Zircon was analyzed in situ for U-Pb and O isotopes using the SHRIMP II at the Beijing SHRIMP Centre, Chinese Academy of Geological Sciences, and for Hf isotopes using the LA-MC-ICP-MS at Hong Kong and Frankfurt Universities (Tables 2 and 3; Tables S1 and S2; Table S4 in Supporting Information S1). The analyses were guided by optical and cathodoluminescence (CL) images (Figures 5–7). Analytical procedures are presented in detail in Supporting Information S1.
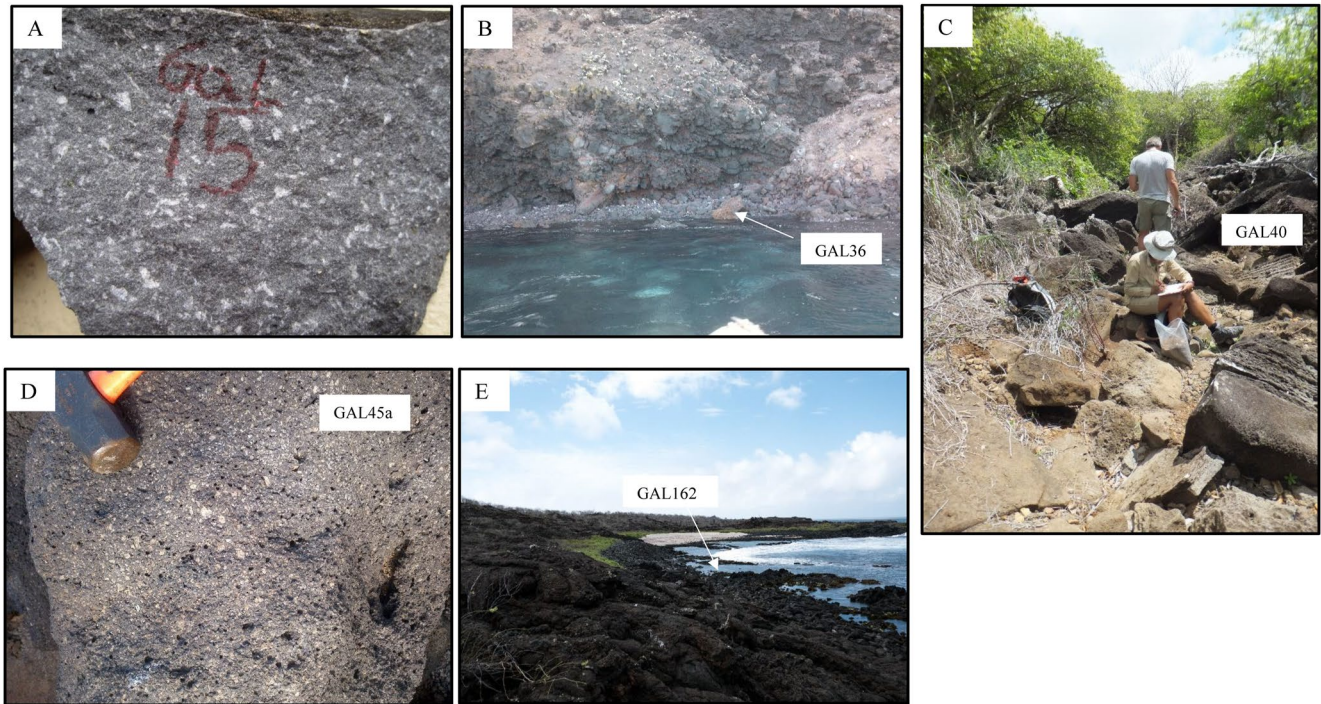
Figure 4. Photos of some rock samples and locations from where samples that contain zircons were collected. See Table 1 for sample coordinates and Table S1 for sample geochemistry. (a) Sample GAL15 is a porphyritic basalt with plagioclase phenocrysts collected at Las Grietas south of Santa Cruz, (b) Sample GAL36 was collected in a rocky cliff from western Pinzón, the sample is a porphyritic basalt with abundant plagioclase phenocrysts up to 6 mm long, (c) GAL40 is a vesicular basalt with olivine phenocryst collected in a dry stream west of Puerto Vaquerizo Moreno (San Cristobal), (d) GAL45a is a vesicular basalt with plagioclase phenocryst collected in the NW coast of Santa Fe, (e) GAL162 is a porphyritic basalt with olivine phenocrysts (up to 5 mm in length) collected at La Loberia, western Floreana.

2.3. Geodynamic Modeling Approach

The numerical experiments were performed using LaMEM (Kaus et al., 2016; Piccolo et al., 2020), a visco-elasto-plastic finite difference code. LaMEM solves the fundamental conservation equations of mass (Equation 1), momentum (Equation 2), and energy (Equation 3), assuming the rocks to be incompressible:

$$\frac{\partial v_i}{\partial x_i} = 0 \tag{1}$$

$$\frac{\partial \tau_{ij}}{\partial x_j} - \frac{\partial P}{\partial x_i} + \rho g = 0 \tag{2}$$

$$\rho C_p \frac{DT}{Dt} = \frac{\partial}{\partial x_i}\left(k\frac{\partial T}{x_i}\right) \tag{3}$$

where v_i are the components of the velocities along the x_i direction, τ_{ij} are the components of the deviatoric stress tensor, P is the pressure, g is the gravitational acceleration and ρ is the density. DT/Dt is the substantial time derivative of the temperature, C_p is the heat capacity, k is the thermal conductivity.

The conservation equations are solved in a fixed Eulerian frame of reference, using a finite difference staggered grid scheme, while the advection is explicit with time and performed using Lagrangian particles and a second order Runge Kutta scheme. The Lagrangian particles carry all the historical information needed to solve the equations.

2.3.1. Numerical Design

The main goal of our simulations is to understand if plume-lithosphere interaction is able to generate chemically distinct mantle domains that preserves geochronological information for a sufficiently long period of time (i.e., >80 Myrs). Furthermore, we want to assess if some of these chemical heterogeneities can be captured again by

Table 1
Sample Location, Rock Samples Are Designated in Bold Letters

Island	Field number	Geographic coordinates		Location	Sample
Santa Cruz	GAL3	S00°45′49.56″	W090°20′25.14″	Tortuga Bay	Beach sand
	GAL6	S00°39′34.8″	W090°16′09.3″	Cascajo cave	Lava tube deposit
	GAL15	**S00°45′24.7″**	**W090°18′56.3″**	**Las Grietas**	**Basalt**
	GAL16	S00°39′34.8″	W090°16′09.3″	Cascajo cave	Lava tube deposit
	GAL17	S00°29′48.5″	W090°17′51.8″	Las Bachas beach	Beach sand
Baltra	GAL56	S00°26′05.8″	W90°16′58.1″	La marina Beach	Beach sand
	GAL86	S00°28′26.2″	W90°15′40.8″	SE of Baltra Island at canal Itabaca	Beach sand
Floreana	FL-6	S01°16′34.6″	W90°29′17.4″	Playa Negra	Beach sand
	FL-7	S01°14′12.78″	W90°27′0.77″	Post Office beach	Beach sand
	FL-8	S01°15′44.1″	W90°22′15.7″	Las Cuevas beach	Beach sand
	GAL70	S01°16′34.4″	W90°29′17.2″	Playa Negra	Beach sand
	GAL140	S01°14'11.7″	W90°26′57.2″	Post Office beach	Beach sand
	GAL147	S01°13′40.85″	W90°25′25.62″	Punta Cormoránt	Beach sand
	GAL149	S1°15′39.52″	W90°22′12.24″	Las Cuevas beach	Beach sand
	GAL155	S01°15′57.79″	W90°29′15.64″	North of Puerto Velazco	Beach sand
	GAL162	**S01°17′13.83″**	**W90°29′44.17″**	**La Lobería**	**Basalt**
	GAL172	S01°17′36.72″	W90°29′41.68″	South of La loberia	Beach sand
	GAL183	S01°15′44.1″	W90°22′15.7″	Cueva de los piratas stream	Streambed deposit
	GAL197	S01°15′40.23″	W90°26′07.28″	Stream coming down Cerro Ventana to Post Office	Streambed deposit
San Cristobal	SCR-2	S00°53′26.6″	W89°36′43.53″	Cabo de Horno beach at Carola point	Beach sand
	SCR-3	S00°55′32.5″	W89°25′47.7″	Puerto Chino	Beach sand
	SCR-5	S00°55′30.09"	W89°36′50.40"	La Loberia	Beach sand
	GAL40	**S00°54′29.60″**	**W89°36′20.43″**	**Dry streambed**	**Basalt**
Rábida	GAL28	S00°24′14.8″	W90°42′11.2″	NE of Rabida	Beach sand
	GAL29B	**S00°24′14.8″**	**W90°42′11.4″**	**NE of Rabida**	**Basalt**
Isabela	**GAL30**	**S00°23′32.1″**	**W90°59′44.0″**	**Volcán Alcedo**	**Basalt**
	GAL120	**S00°24′30.30″**	**W90°59′13.30″**	**Volcan Alcedo, close to Punta Alfaro,**	**Pumice**
	GAL122	S00°24′25.0″S	W90°59′2.19″	Volcano north of Punta Alfaro	Beach sand
Pinzón	**GAL36**	**S00°36′10.0″**	**W90°38′54.7″**	**Western coast**	**Basalt**
	GAL38	S00°36′10.0″	W90°38′54.7″	Western coast	Beach sand
Santa Fé	GAL43	S00°48′17.7″	W90°05′09.3″	NW coast	Beach sand
	GAL45a	**S00°48′17.7″**	**W90°05′09.3″**	**NW coast**	**Basalt**
	GAL47	S00°48′9.53″	W90° 2′26.93″	Barrington Bay	Beach sand
	GAL48	S00°48′13.9″	W90°02′27.9″	Barrington Bay	Beach sand
	GAL230	S00°49′34.22″	W90°01′45.37″	Punta del miedo	Beach sand
Española	GAL53	S01°21′15.32″	W89°39′34.64″	Gardner Bay	Beach sand
Genovesa	GAL54	N00°19′6.42″	W89°56′57.81″	Genovesa Bay	Beach sand

the mantle plume during a later model stage. For simplification, we do not consider the effects of radiogenic, adiabatic, and shear heating. We employ lateral inflow-outflow boundary conditions to simulate the motion of the oceanic plate, as well as a plume inflow bottom boundary condition. To identify the potential domains that undergo partial melting and chemical refinement, we interpolate the volumetric melt fraction (ϕ) and solid density (ρ_{solid}) from a precomputed mantle petrological phase diagram.
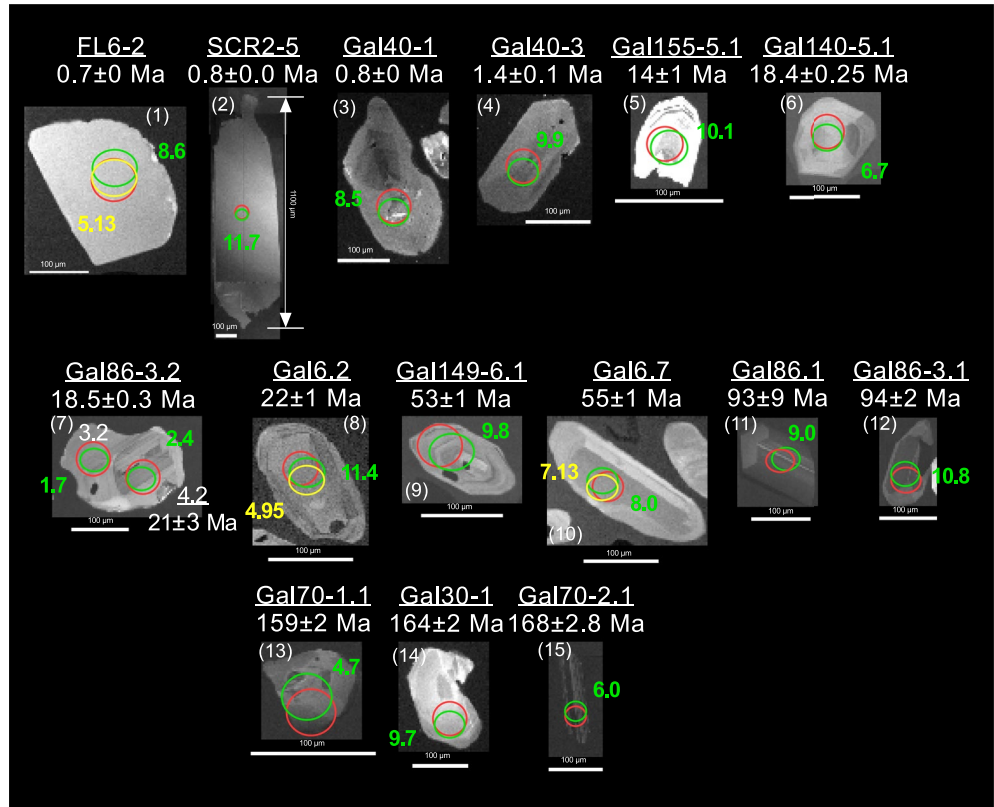
Figure 5. Cathodoluminiscence (CL) images of the most representative Galapagos Plume Array (GPA) zircon grains (0–164 Ma). Red circles represent SHRIMP spots while green and yellow circles represent Hf and δ18O spots, respectively. Scale bars in white (100 μm).

Density depends on temperature and volumetric melt fraction:

$$\rho_{\text{solid}} = \rho_0 \left(1 - \alpha \left(T - T_{\text{ref}}\right)\right) \tag{4}$$

$$\rho_{\text{eff}} = \rho_{\text{solid}}(1 - \phi) + \rho_{\text{melt}}\phi \tag{5}$$

where ρ_{eff} is the effective density, ρ_{solid} is the solid density, ρ_{melt} is the melt density, α is the thermal expansion coefficient, T is the actual temperature and T_{ref} is the reference state temperature. We assume that most melt that forms in the mantle is rapidly extracted and that only a maximum amount of melt can remain in the mantle, which is why $\phi = 0.08$ is taken as an upper bound in Equation 5. The mantle phase diagram has been computed using Perple_X (Connolly, 2009) using the pyrolite composition from McDonough and Sun (1995), and the solution model of Jennings and Holland (2015) see also Piccolo et al. (2020). All the relevant properties of each of the compositional phases are listed in Table S5 in Supporting Information S1.

We employ a purely viscous constitutive relationship in this study where the deviatoric strain rate, $\dot{\varepsilon}_{ij} = \frac{1}{2}\left(\frac{\partial v_i}{\partial x_j} + \frac{\partial v_j}{\partial x_i}\right)$ consists of a combination of diffusion and dislocation creep and:

$$\dot{\varepsilon}_{ij} = \frac{\tau_{ij}^{\text{shear}}}{2\eta_{\text{eff}}} = \dot{\varepsilon}_{ij}^{\text{diff}} + \dot{\varepsilon}_{ij}^{\text{disl}} + \dot{\varepsilon}_{ij}^{\text{upper}} \tag{6}$$

where η_{eff} is the effective creep viscosity. The viscosity of the diffusion and dislocation creep mechanisms are given by

$$\eta_{\text{diff}} = \frac{1}{2} B_{\text{diff}}^{-1} \exp\left(\frac{E_{\text{act}}^{\text{diff}} + PV_{\text{act}}^{\text{diff}}}{RT}\right),$$
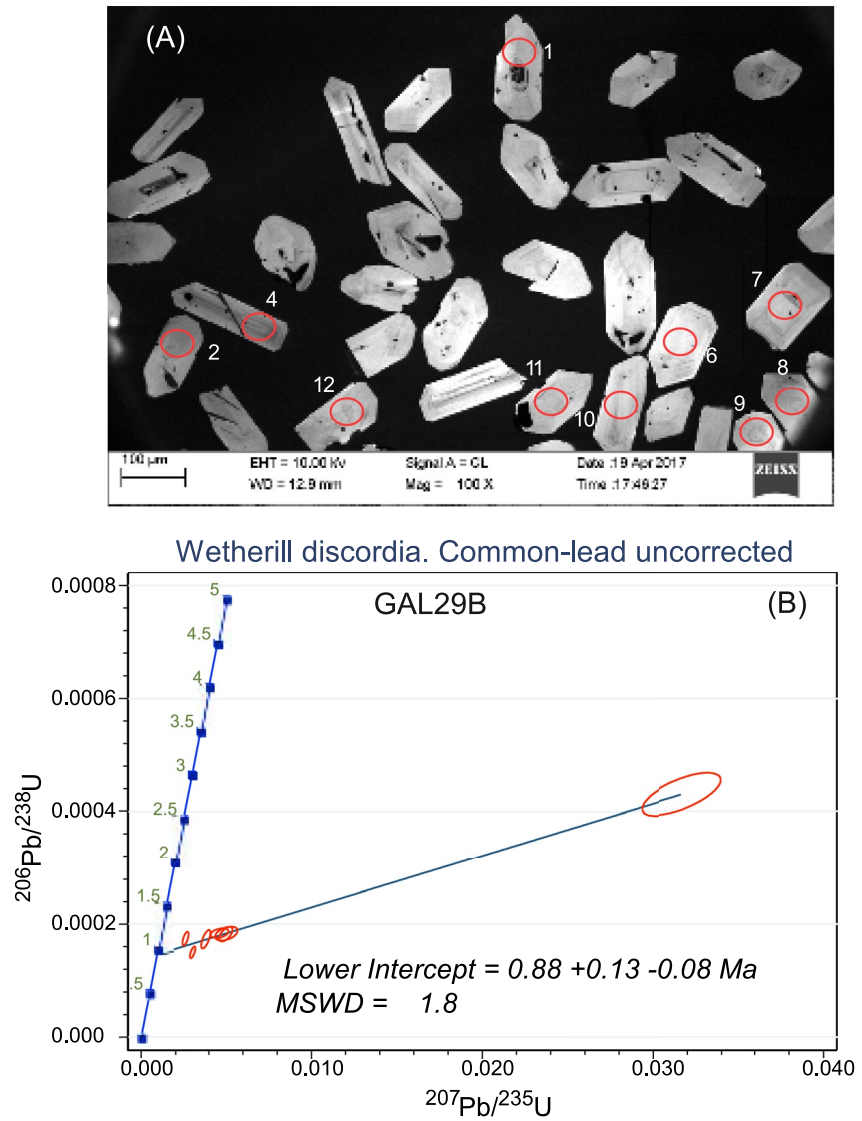
Figure 6. (a) Cathodoluminiscence (CL) image with dated spots (a) and Wetherill Discordia diagram (b) of zircon grains from sample GAL29B.

$$\eta_{disl} = \frac{1}{2} B_{disl}^{-1/n} \left(\dot{\varepsilon}_{II}^{disl} \right)^{\frac{1}{n}-1} \exp\left(\frac{E_{act}^{disl} + P V_{act}^{disl}}{RT} \right), \tag{7}$$

whereas the linear viscous upper cutoff η_{upper} is constant and the second invariant of the strain rate tensors and deviatoric stress tensors are given by $\dot{\varepsilon}_{II} = (0.5 \dot{\varepsilon}_{ij} \dot{\varepsilon}_{ij})^{0.5}$, and $\tau_{II} = \left(0.5 \tau_{ij}^{shear} \tau_{ij}^{shear} \right)^{0.5}$ respectively. B_{diff} and B_{disl} are the pre-exponential factor of diffusion and dislocation creep respectively, n the stress exponent, $\dot{\varepsilon}_{II}$ the second invariant of the strain rate tensor, and E_{act} and V_{act} are the activation energy and volume respectively (see Table S5 in Supporting Information S1).

By substituting Equation 7 into Equation 6 and using the square root of the second invariant of strain rate and stress, Equation 6 can be expressed as:

$$\dot{\varepsilon}_{II} = \frac{\tau_{II}}{2\eta_{diff}} + \frac{\tau_{II}}{2\eta_{upper}} + \left(\frac{\tau_{II}}{2\eta_{disl,0}} \right)^n \tag{8}$$
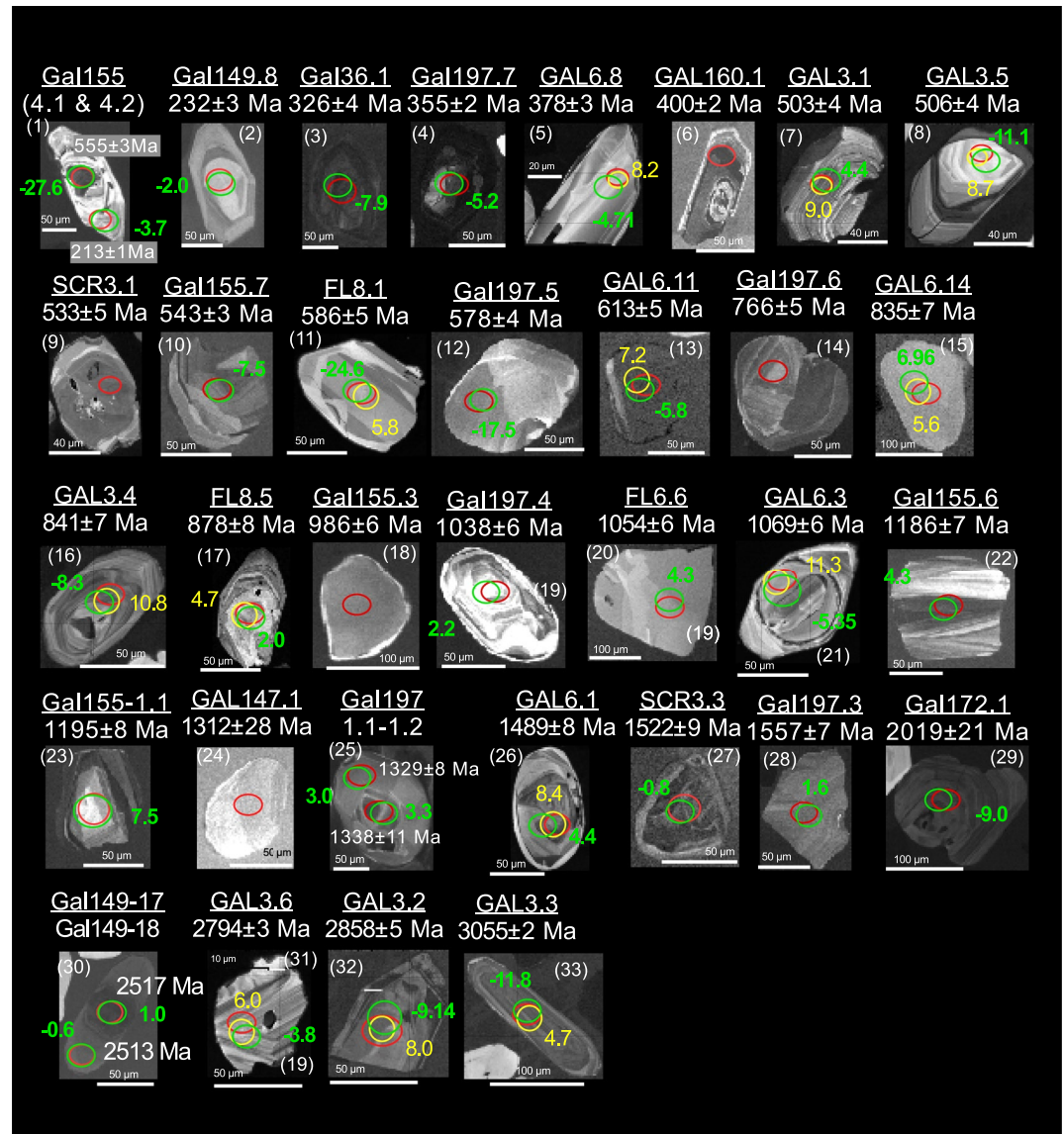
Figure 7. Cathodoluminiscence (CL) images of the most representative older zircon grains (>200 Ma). Red circles represent SHRIMP spots while green and yellow circles represent Hf and δ18O spots, respectively. Scale bars in white.

where $\eta_{disl,0}$ is the strain rate independent part of η_{disl}.

Equation 8 is a nonlinear expression of τ_{II}, which is solved using (local) Newton iterations. The total deviatoric stress tensor also contains a lower cutoff viscosity that is added in a Kelvin-like manner:

$$\tau_{ij} = \tau_{ij}^{\text{shear}} + 2\eta_{\text{lower}}\dot{\epsilon}_{ij} \tag{9}$$

Equation 9 is substituted in the force balance equation (Equation 2), which gives a set of nonlinear equations, which is solved with a Newton solver preconditioned with Picard iterations.

2.3.2. Initial Setup and Boundary Condition

The reference scenario of our 2D/3D thermo-mechanical numerical simulations (Figure 8) features a plume with a radius of 150 km and an excess temperature of 250°C with respect to the local mantle potential temperature, consistent with recent estimates from seismic tomography (Nolet et al., 2019). The plate has a constant velocity of 5 cm/yr, and an initial thermal age of 30 Ma (see Section 2.3 and Supporting Information S1 for further details).
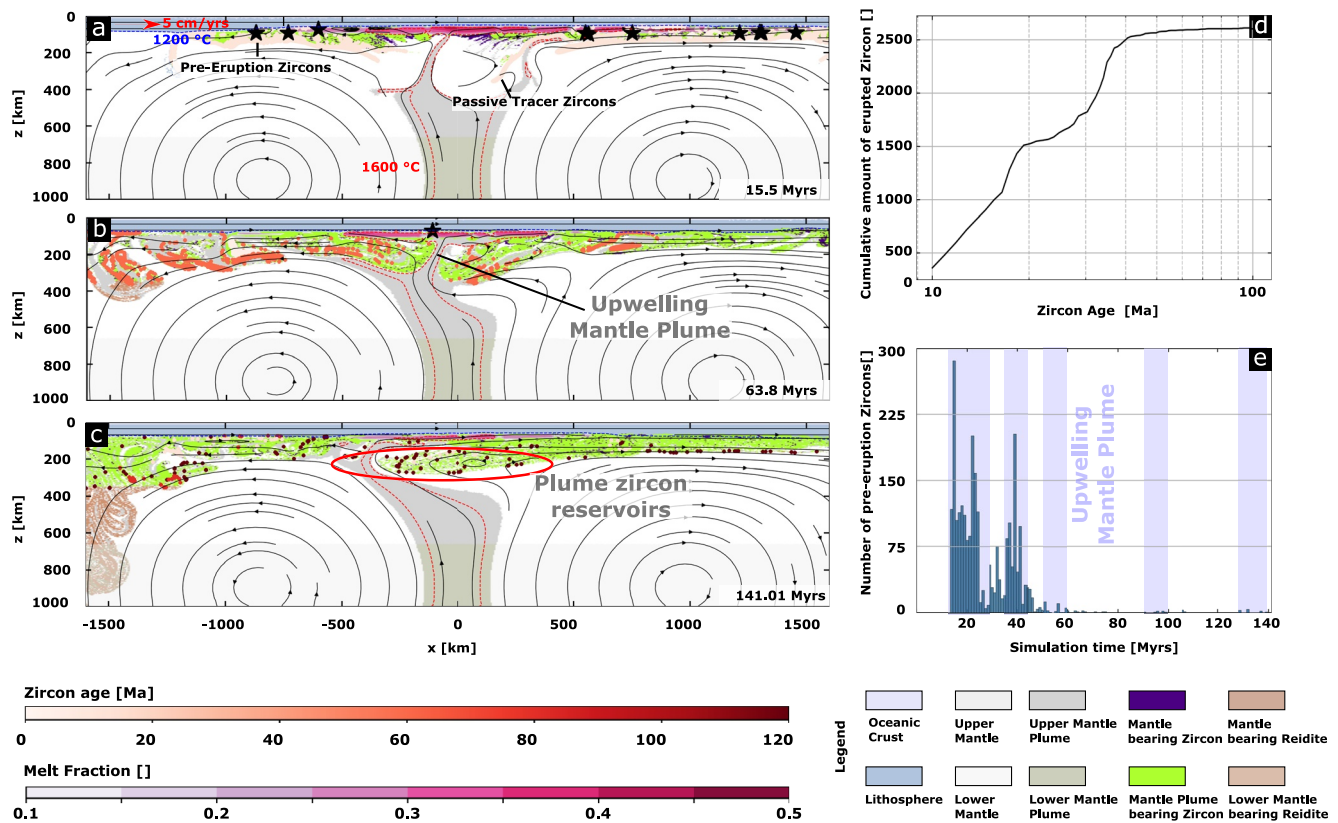
Figure 8. Numerical models of plume-lithosphere interaction. Snapshots (a–c) show the dynamics of a plume (with 1,600°C) interacting with a 30 Myrs old oceanic lithosphere that moves with 5 cm/yr to the right. Thin lines with arrows are streamlines indicating flow directions; the arrows are unscaled as they would otherwise be dominated by the plume velocities. Partially molten regions (indicated by purple shaded areas produce chemically distinct mantle domains (green/violet). We additionally highlight the chemical heterogeneous mantle domain that undergoes the zircon-reidite phase transition. The pathway of zircons in the mantle is tracked by passive tracer zircons (circles) which are colored by age until a zircon arrives at a partially molten region for the second time when they are removed from the numerical domain (indicated by stars). (d) Cumulative distribution of erupted zircons. Ages <10Ma are absent because it takes some time for the initial plume to arrive at the lithosphere-asthenosphere boundary (and melt) and because we only plot zircons that arrive at the melting zone for the second time. (e) Temporal evolution of erupted passive tracer zircons along with periods of plume activity, which show that some old zircons can be preserved in the shallow mantle for extended periods of time.

For the 2D numerical experiments we used a domain that extends 4,000 km × 1,000 km along the x and z directions and with a grid resolution of 256 × 128 elements respectively. This strategy allows performing long-term experiments able to cover the time evolution recorded by the geochemical data here presented. Moreover, employing such large numerical domains prevents inflow boundary condition to interfere with the processes that we simulate. The mantle is initially isothermal (1,350°C) using the half-space cooling model to describe the initial lithospheric thermal structure. The uppermost portion of the compositional field is composed of a thin oceanic crust (10 km), and 90 km of lithospheric mantle, while the rest of the domain is filled with mantle phases (i.e., upper and lower mantle). The thickness of the lithospheric mantle is self-adjusting during the evolution of the simulation as a function of the 1,200°C isotherm position. A depth dependent post-spinel phase transition at 660 km is introduced to adjust the inflow velocity of the plume allowing it to have a smooth temperature profile (the density jump associated with this phase transition is $\Delta\rho = 300$ kg/m^3 see Table S5 in Supporting Information S1). The initial plume is located at the bottom of the numerical domain and in its centre. In most numerical experiments (Table S6 in Supporting Information S1), we introduce a rectangular thermal perturbation at the bottom to simulate an initial plume conduit to trigger the upwelling at the onset of the simulation, which has the same phases as the plume and an excess temperature of 250°C. Its width is equal to the inflow diameter (i.e., 300 km) and covers almost all the lower mantle with its height. Since many of the zircons that have been collected from Galápagos are older than the Nazca plate, we assume that the Pacific plate retains its integrity for the whole duration of the simulation. The initial age of the plate, and the corresponding temperature of the inflow boundary condition is varied from 15 to 40 Myrs and the plate velocity is varied from 1 to 10 cm/yr.

We employ a free slip boundary condition at the upper boundary with a constant surface temperature of 0°C. Lateral boundaries are no-heat flux and free slip boundary condition except for a narrow inflow-outflow window. The inflow-outflow window extends from the top of the domain to a minimum depth of 100 km to a maximum of 350 km. In all numerical experiments the velocity between 0 and 100 km along z-direction is constant, and directed from left to right side of the numerical domain. In most of the numerical experiments we introduce a buffer inflow-outflow window in which the velocity is linearly decreased to 0 km (this distance is varied from 0 to 250 km). The inflow plate has a constant thermal age that increases toward the right as a function of the plate velocity. In some simulations, we also employ a stress-free lateral boundary with lithostatic pressure (see Supporting Information S1). The bottom boundary is permeable with no tangential velocity components (Ribe & Christensen, 1994, 1999), and the temperature at the boundary is constant and equal to the ambient mantle temperature (1,350°C) with a Gaussian thermal perturbation with a radius of 150 km and a $\Delta T = 250$°C. Within the plume inflow window (−150, 150 km along x direction), particles with plume phase are injected with a temperature equal to the one of the bottom boundary condition. Outside this inflow window, the temperature of the material is assumed to be equal to the ambient mantle temperature and has the same phase of the normal mantle.

2.3.3. Mantle Chemical Heterogeneities

In order to track the mantle chemical heterogeneities, we use two strategies: first, we highlight areas of the mantle or plume that reaches $\phi = 0.05$ at least once (Piccolo et al., 2019); second, we activate passive tracers ("passive tracers zircon" in Figure 8) that are associated with a chemical heterogeneous mantle domain and start tracking their position, temperature, pressure and melt quantity. The initial position of the passive tracers is defined by a refined grid spanning from −1,200 to 1,200 km and from 100 to 200 km along x and z direction respectively. As soon as they are activated, we record the age of the melting event, assuming that this portion of mantle could bear geo-chronological information (see Figure 8). These mantle domains have to be interpreted as potential portions of the mantle that can bear zircon. Once the passive tracers come in a region that undergoes another melting event (when $\phi > 0.05$), we assume that the rising melts will bring the zircons rapidly to the surface and remove them from the model domain ("pre-eruption zircons" in Figure 8). When the passive tracer is erupted, we collect information about the zircon age, and the timing at which the eruption event occurs (see Figure 8). The age of the potential zircon generated during the partially melting of the mantle is measured in Ma, while the actual simulation time is expressed in Myrs (as for the initial thermal age of the lithosphere). The chemical heterogeneous mantle domains that are tracked give an estimation of the age of the event that may lead to the generation of zircon population and represents an estimation of the maximum age retained by them.

3. Results

The largest concentration of all zircon grains in the Archipelago occurs in Floreana representing 37%, followed by Santa Cruz (14%), San Cristobal (13%) and Baltra (9%). The rest of the islands have more or less a similar distribution of 6% with the lowest concentration in Genovesa and Pinzón (Figure 2). This distribution, however, is to some extent biased by sampling density of each island which was in general a function of the number of sandy beaches present on each island, accessibility to the beaches etc. The chemical composition of the zircon bearing rock samples is displayed in Figure 9 and Table S3 in Supporting Information S1.

The U-Pb age of most grains (74%) is <4 Ma old, within the range but ~1.2 Million year older than the K-Ar ages (~2.8 Ma) reported by White et al. (1993) which corresponds to the age of basaltic to rhyolitic magmatism in the islands (Geist et al., 2014; Stock et al., 2020) (Figures S1 and S2 in Supporting Information S1). According to our data the volcanoes in Galapagos do not form a linear progressive chain as noticed by White et al. (1993) nevertheless the islands in the eastern part of the Archipelago (Santa Fé, Espanola, Floreana, San Cristobal and Santa Crúz) are consistently older than the ones in the west (Rábida, Baltra and Isabela) (Figure 2). A detailed study of the age of the islands is in preparation, however the age ranges (<4 Ma) in the islands is as follow: Santa Fé: 1.6 to 3.93 Ma, Espanola: ~0.5 to 2.31 Ma, Floreana: ~0.20 to 3.81 Ma, San Cristobal: ~0.52 to 2.10 Ma, Santa Cruz: ~0.05 to 3.50 Ma (with one grain ~4.0 Ma), Rábida:~ 0.5 to 1.09 Ma, Baltra: ~0.04 to 1.50 Ma, and Isabela: ~0.00 to 1.22 Ma (Table 2). This data indicates that the very young zircon population crystallized from the evolving basaltic liquids upon cooling and that the detrital grains younger than 4 Ma derive from erosion of the volcanic rocks exposed in the islands. Twenty of these samples, however, contain zircon grains older than
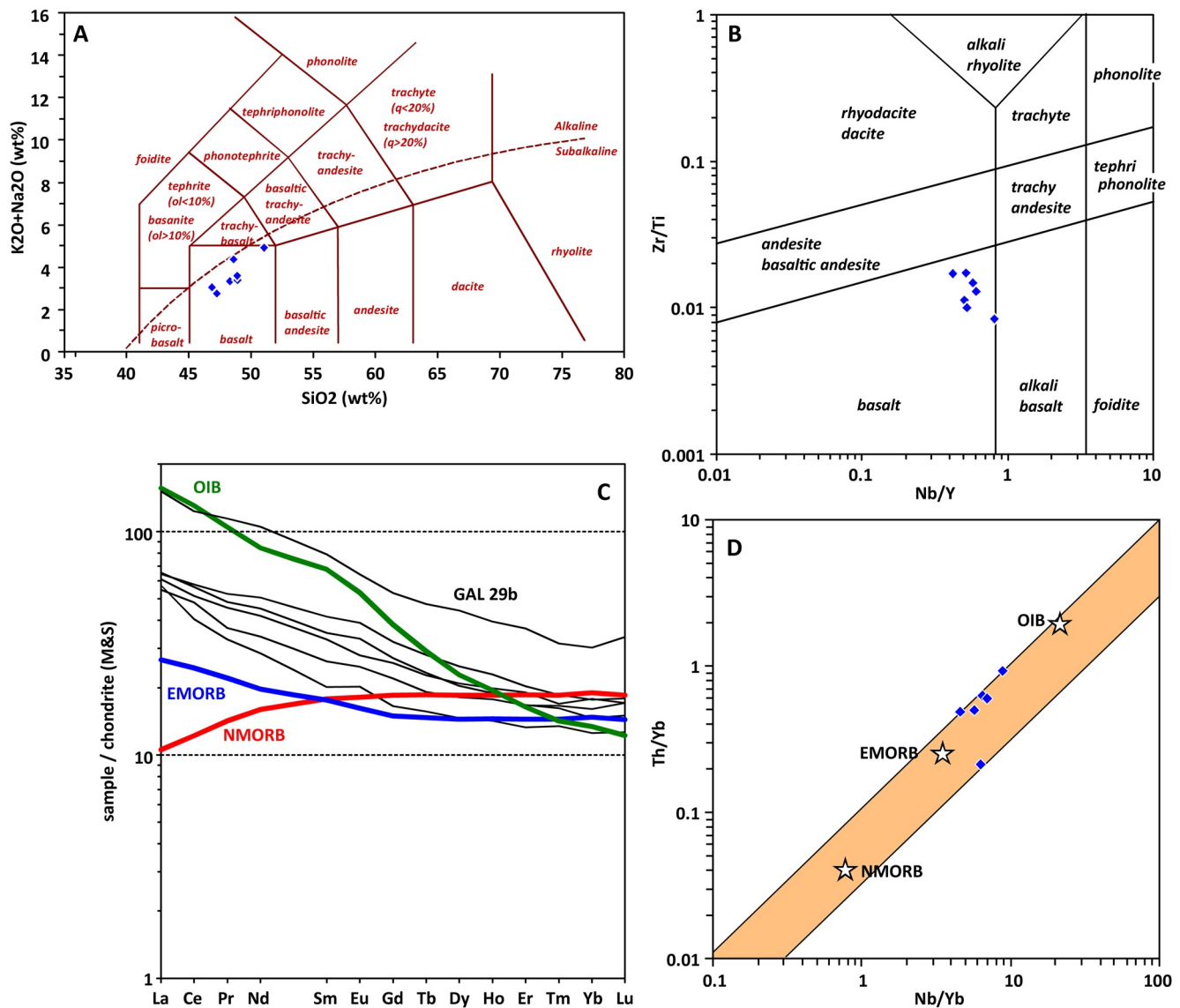
Figure 9. Chemical composition of zircon-bearing rock samples shown in Figure 2. (a) TAS classification diagram after (Bas et al., 1986). (b) Zr/Ti versus Nb/Y (Pearce, 1996). (c) Chondrite (CI)-normalized (McDonough & Sun, 1995) REE abundances. (d) Nb/Yb versus Th/Yb of the analyzed samples including the MORB-OIB array (Pearce, 2014). In all diagrams, reference normal and enriched mid-ocean ridge basalts (N-MORB and E-MORB, respectively) and ocean island basalt (OIB) (Sun & McDonough, 1989).

14 Ma (Tables 2 and 3) that significantly predate the emergence of any existing island, as well as initiation of the GSC and associated lithosphere (10 Ma).

The zircon grains with ages less than 4 Ma and up to 164 Ma define what we call the Galápagos Plume Array (GPA). Most of the zircons are generally anhedral to subhedral, which can be explained because most were retrieved from beach sands (Figure 5). Some grains appear broken and there is a diversity in shape. Few grains are euhedral and in general all grains range in size from ∼80 to 300 μm with some bigger grains of more than 1 mm (Figures 5 and 6). The grain interiors exhibit relatively high CL intensity and are mostly homogenous with some grains displaying weak to well-developed magmatic zonation. Zircons from basaltic sample GAL29B are perfectly euhedral ranging in size from 150 to more than 200 μm and are also characterized by high CL intensity and oscillatory zoning typical of magmatic zircon (Figure 6a). The grains have high positive $\varepsilon Hf_{(t)}$ (6.9–10.6; Table S2) and young ages of 0.88 ± 0.08 Ma, indicating growth upon crystallization of evolved basaltic liquid (Figure 6b).

Table 2
SHRIMP II Analytical Data for Spot Analyses of Young Zircons From Galápagos

Sample no.	Coordinates	Location	U ppm	Th ppm	Th/U	f206_8 %	206Pb/238U	±err	208Pb/232Th	±err	206/238 Age	± 1s	208/232 Age	± 1s	Best age Age (Ma)	±1s	$\varepsilon Hf_{(t)}$	$\delta^{18}O_{SMOW}$	±
Santa Cruz																			
GAL3 (beach sand)																			
GAL3.7	S00°45′49.56″	Tortuga Bay	164.3	97.6	0.59	33.4	0.00006	0.00002	0.00009	0.00000	0.41	0.12	1.91	0.04	0.41	0.12	7.1	4.70	0.07
GAL3.8			144.6	154.1	1.07	82.5	0.00006	0.00002	0.00011	0.00003	0.38	0.15	2.24	0.70	0.38	0.15	7.9	5.37	0.07
GAL3.9			869.8	1,599.3	1.84	.	0.00004	0.00000	0.00002	0.00000	0.27	0.00	0.50	0.01	0.27	0.01		5.17	0.13
GAL3.10			115.2	66.0	0.57	94.7	0.00010	0.00005	0.00036	0.00017	0.63	0.34	7.33	3.45	0.63	0.34	8.1	4.33	0.12
GAL3.12			389.6	470.4	1.21	27.2	0.00007	0.00002	0.00005	0.00001	0.48	0.12	0.98	0.25	0.48	0.12	10.8	5.33	0.09
GAL3.13			154.8	134.5	0.87	57.6	0.00005	0.00000	0.00010	0.00001	0.35	0.02	1.94	0.14	0.35	0.02	7.6	4.87	0.10
GAL6 (lava tube deposit)	S00°39′34.8″ W090°16′09.3″	Cueva Cascajo																	
GAL6-4			71.1	30.2	0.43	12.3	0.00092	0.00006	0.00081	0.00002	5.97	0.38	16.30	0.45	5.97	0.38	11.4	6.54	0.07
GAL6-5			144.3	80.1	0.55	80.8	0.00001	0.00002	0.00006	0.00003	0.08	0.12	1.15	0.50	0.08	0.12	9.3	5.00	0.15
GAL6-9			161.6	209.2	1.30	32.7	0.00010	0.00002	0.00008	0.00001	0.67	0.11	1.56	0.23	0.67	0.11	10.6	4.65	0.17
GAL6-12			497.1	404.3	0.81	0.0	0.00049	0.00004	0.00016	0.00001	3.13	0.25	3.14	0.13	3.13	0.25	8.6	5.47	0.11
GAL6-13			179.0	135.4	0.76	100.3	0.00003	0.00002	0.00011	0.00003	0.22	0.12	2.15	0.53	0.22	0.12	8.8	4.75	0.05
GAL6-15			45.7	19.9	0.44	133.0	0.00001	0.00001	0.00006	0.00006	0.05	0.10	1.22	1.25	0.05	0.10	11.0	5.18	0.14
GAL15 (Basalt)	S00°45′24.7″ W090°18′56.3″	Las Grietas																	
GAL15-1			39.5	30.4	0.77	98.2	0.00062	9.69219	0.00017	347.40500	4.00	1.00	3.40	12.00	4.00	1.00	8.2		
GAL15-2			195.1	161.7	0.83	49.4	0.00054	5.05569	0.00031	24.06600	3.50	0.60	6.20	1.00	3.50	0.60	5.6		
GAL16 (Lava Tube deposit)	S00°39′34.8″ W090°16′09.3″	Cueva Cascajo																	
GAL16-1			151.0	84.1	0.56	28.3	0.00003	0.00000	0.00006	0.00002	0.21	0.01	1.17	0.45	0.21	0.01		4.05	0.13
GAL17 (Beach sand)	S00°29′48.5″ W090°17′51.8″	Las Bachas Beach																	
GAL17-1			48.5	27.9	0.58	4.4	0.00014	0.00004	0.00006	0.00001	0.90	0.24	1.24	0.28	0.90	0.24	12.0	6.26	0.10
GAL17-2			1,105.9	1,030.6	0.93	8.0	0.00006	0.00002	0.00003	0.00000	0.37	0.11	0.58	0.03	0.37	0.11	9.4	5.15	0.12
GAL17-3			124.9	68.3	0.55	49.2	0.00005	0.00001	0.00013	0.00004	0.36	0.07	2.66	0.82	0.36	0.07	7.2	5.62	0.18
GAL17-4			116.9	63.3	0.54	29.6	0.00005	0.00001	0.00013	0.00004	0.29	0.09	0.18	0.13	0.29	0.09	9.8		
GAL17-5			55.2	39.5	0.72	30.1	0.00021	0.00003	0.00024	0.00001	1.37	0.21	4.84	0.12	1.37	0.21	12.2		
Baltra																			
GAL56 (Beach sand)	S00°26′05.8″ W90°16′58.1″	La Marina Beach																	

Table 2
Continued

Sample no.	Coordinates	Location	U ppm	Th ppm	Th/U	f206_8 %	206Pb/238U	±err	208Pb/232Th	±err	206/238 Age	±1s	208/232 Age	±1s	Best age Age (Ma)	±1s	εHf(t)	±1s	δ18O$_{SMOW}$	±
GAL56-1			113.1	59.4	0.53	2.4	0.00009	0.00002	0.00004	0.00001	0.59	0.12	0.78	0.29	*0.59*	*0.12*	8.8			
GAL56-2			46.0	24.6	0.53	−9.1	0.00014	0.00003	0.00004	0.00001	0.93	0.22	0.78	0.29	*0.93*	*0.22*	11.1			
GAL56-3			281.6	312.3	1.11	−3.3	0.00019	0.00000	0.00005	0.00001	1.24	0.03	1.03	0.11	*1.24*	*0.03*	11.9			
GAL56-4			106.0	57.2	0.54	.	0.00003	0.00003	0.00003	0.00000	0.23	0.19	0.63	0.10	*0.23*	*0.19*	9.3			
GAL56-5			51.3	27.3	0.53	9.9	0.00014	0.00007	0.00009	0.00001	0.89	0.44	1.89	0.29	*0.89*	*0.44*	11.3			
GAL56-6			85.3	42.3	0.50	12.5	0.00023	0.00002	0.00018	0.00008	1.50	0.15	3.74	1.67	*1.50*	*0.15*	12.0			
GAL56-7			92.4	56.5	0.61	25.6	0.00019	0.00001	0.00021	0.00005	1.20	0.03	4.21	0.96	*1.20*	*0.03*	10.4			
GAL86 (Beach sand)	S00°28′26.2″ W90°15′40.8″	SE of Baltra Island at canal Itabaca																		
GAL86-2.1			1,862	3,126	1.68	.	0.00000	0.00000	0.00001	0.00000	0.04	0.01	0.22	0.03	*0.04*	*0.01*	6.6			
GAL86-5.1			531.0	463.4	0.87	35.2	0.00004	0.00000	0.00006	0.00000	0.29	0.00	1.23	0.10	*0.29*	*0.00*	10.7			
GAL86-6.1			213.9	127.1	0.59	83.7	0.00004	0.00000	0.00018	0.00000	0.29	0.00	3.55	0.06	*0.29*	*0.00*	8.4			
GAL86-7.1			763.5	688.0	0.90	29.9	0.00007	0.00002	0.00006	0.00000	0.45	0.11	1.26	0.01	*0.45*	*0.11*	10.3			
GAL86-8.1			50.1	24.7	0.49	135.0	0.00008	0.00001	0.00053	0.00005	0.54	0.09	10.61	1.05	*0.54*	*0.09*	11.8			
GAL86-9.1			1,383.6	1,738.9	1.26	33.0	0.00007	0.00000	0.00005	0.00000	0.47	0.02	1.09	0.01	*0.47*	*0.02*	8.6			
GAL86-10.1			150.9	94.6	0.63	31.4	0.00006	0.00000	0.00009	0.00000	0.41	0.01	1.84	0.07	*0.41*	*0.01*	9.5			
GAL86-11.1			145.4	84.7	0.58	.	0.00006	0.00002	0.00007	0.00000	0.37	0.12	1.38	0.03	*0.37*	*0.12*	8.8			
GAL86-12.1			249.8	172.4	0.69	27.5	0.00006	0.00000	0.00007	0.00000	0.37	0.03	1.49	0.02	*0.37*	*0.03*	8.5			
GAL86-13.1			147.7	87.5	0.59	59.0	0.00004	0.00001	0.00012	0.00000	0.29	0.04	2.47	0.01	*0.29*	*0.04*	9.5			
Pinzón																				
GAL38 (Beach sand)	S00°36′10.0″ W90°38′54.7″	Western coast																		
GAL38–1.1			216.7	118.6	0.55	94.5	0.00004	0.00000	0.00019	0.00000	0.30	0.02	3.82	0.03	*0.30*	*0.02*	9.0			
GAL38–2.1			216.1	128.9	0.60	81.9	0.00005	0.00000	0.00016	0.00000	0.31	0.02	3.15	0.01	*0.31*	*0.02*	9.9			
GAL38–3.1			161.2	91.9	0.57	64.9	0.00004	0.00000	0.00012	0.00000	0.30	0.02	2.37	0.05	*0.30*	*0.02*	8.4			
GAL38–4.1			675.3	681.0	1.01	42.1	0.00005	0.00000	0.00005	0.00000	0.31	0.01	1.12	0.01	*0.31*	*0.01*	9.9			
Floreana																				
FL6 (Beach sand)	S01°16′34.6″ W90°29′17.4″	Playa Negra																		
FL-6.1			144	152	1.06	29.5	0.00015	0.00000	0.00012	0.00001	0.95	0.03	2.50	0.16	*0.95*	*0.03*	11.3			
FL-6.2			177	194	1.10	42.3	0.00005	0.00001	0.00006	0.00001	0.32	0.04	1.20	0.24	*0.32*	*0.04*	11.5			
FL-6.3			76	46	0.60	32.9	0.00037	0.00004	0.00051	0.00003	2.39	0.23	10.34	0.64	*2.39*	*0.23*	9.2			

Table 2
Continued

Sample no.	Coordinates	Location	U ppm	Th ppm	Th/U	f206_8 %	206Pb/238U	±err	208Pb/232Th	±err	206/238 Age	±1s	208/232 Age	±1s	Best age (Ma)	±1s	εHf(t)	δ18O_SMOW	±
FL-6.4			51	91	1.76	79.9	0.00011	0.00004	0.00011	0.00003	0.68	0.25	2.16	0.68	**0.68**	**0.25**	12.9		
FL-6.5			2,313	4,586	1.98	0.1	0.00014	0.00000	0.00005	0.00000	0.92	0.03	0.93	0.03	**0.92**	**0.03**	10.9		
FL-6.6			213	163	0.76	21.1	0.00013	0.00000	0.00011	0.00000	0.86	0.03	2.22	0.10	**0.86**	**0.03**	11.4		
FL6-1			220.4	322.4	1.46	13.8	0.00018	0.00001	0.00009	0.00001	1.18	0.05	1.78	0.26	**1.18**	**0.05**	8.2	5.72	0.10
FL6-2			1,295.7	9,059.9	6.99	74.6	0.00010	0.00000	0.00003	0.00000	0.67	0.02	0.63	0.02	**0.67**	**0.02**	8.6	5.13	0.07
FL6-4			251.6	210.9	0.84	20.7	0.00003	0.00000	0.00003	0.00000	0.21	0.01	0.64	0.08	**0.21**	**0.01**	7.5	3.83	0.16
FL-7 (Beach sand)	S01°14′12.78″ W90°27′0.77″	Post-office beach																	
FL-7.1			216.7	156.7	0.72	61.4	0.00003	0.00002	0.00007	0.00003	0.23	0.13	1.47	0.56	**0.23**	**0.13**	8.0		
FL-7.2			104.5	8.4	0.08	42.2	−0.00001	0.00000	0.00000	0.00000	0.20	0.10	0.20	0.10	**0.20**	**0.10**	12.7		
FL-7.3			83.0	93.3	1.12	64.0	0.00003	0.00001	0.00006	0.00002	0.23	0.08	1.23	0.50	**0.23**	**0.08**	10.4		
FL-7.4			58.8	36.3	0.62	33.0	0.00040	0.00004	0.00052	0.00004	2.56	0.26	10.60	0.87	**2.56**	**0.26**	9.5		
FL-7.5			120.3	49.8	0.41	22.7	0.00034	0.00003	0.00048	0.00003	2.22	0.17	9.77	0.32	**2.22**	**0.17**	10.4		
FL-7.6			653.6	1,060.8	1.62	2.8	0.00014	0.00001	0.00005	0.00001	0.93	0.05	1.02	0.11	**0.93**	**0.05**	9.1		
FL7-1			317.0	345.7	1.09	3.9	0.00045	0.00002	0.00017	0.00002	2.93	0.14	3.51	0.04	**2.93**	**0.14**	7.9		
FL7-2			96.4	66.5	0.69	41.7	−0.00001	0.00000	0.00000	0.00000	0.3	0.10	0.09	0.11	**0.30**	**0.10**	9.4		
FL7-3			57.7	33.7	0.58	67.8	0.00007	0.00003	0.00021	0.00003	0.48	0.17	4.24	0.53	**0.48**	**0.17**	6.8		
FL7-4			180.7	363.7	2.01	15.3	0.00010	0.00001	0.00004	0.00001	0.63	0.05	0.86	0.03	**0.63**	**0.05**	10.7		
FL8 (Beach sand)	S01°15′44.1″ W90°22′15.7″	Las Cuevas beach																	
FL8.2.1			158.8	152.8	0.96	16.7	0.00020	0.00003	0.00013	0.00001	1.32	0.22	2.53	0.30	**1.32**	**0.22**	10.5		
FL8.3			2,637.6	6,580.2	2.49	1.4	0.00011	0.00000	0.00004	0.00000	0.69	0.01	0.72	0.03	**0.69**	**0.01**	10.5	4.38	0.13
FL8.4			241.7	128.0	0.53	10.8	0.00045	0.00000	0.00032	0.00003	2.88	0.03	6.42	0.60	**2.88**	**0.03**	8.9		
FL8.12			741.7	3,281.0	4.42	6.1	0.00013	0.00000	0.00004	0.00000	0.84	0.02	0.88	0.05	**0.84**	**0.02**	9.8		
FL8.13			189.6	79.1	0.42	6.3	0.00050	0.00002	0.00030	0.00003	3.22	0.09	6.10	0.55	**3.22**	**0.09**	10.1		
FL8.15			421.5	352.4	0.84	3.6	0.00048	0.00001	0.00019	0.00001	3.08	0.05	3.86	0.21	**3.08**	**0.05**	9.1		
FL8.16			43.4	13.8	0.32	44.6	0.00059	0.00014	0.00183	0.00032	3.81	0.90	36.90	6.45	**3.81**	**0.90**	9.3	4.88	0.11
FL8.19			52.2	43.2	0.83	25.7	0.00046	0.00005	0.00041	0.00002	2.98	0.34	8.30	0.39	**2.98**	**0.34**	9.4	4.73	0.11
FL8.20			39.9	27.5	0.69	36.0	0.00042	0.00002	0.00054	0.00006	2.72	0.13	10.99	1.24	**2.72**	**0.13**	8.9		
FL8.21			96.5	71.1	0.74	20.6	0.00055	0.00005	0.00046	0.00005	3.53	0.29	9.31	1.11	**3.53**	**0.29**	8.2	4.52	0.18
FL8.22			654.6	331.4	0.51	3.6	0.00046	0.00001	0.00021	0.00001	3.00	0.10	4.32	0.36	**3.00**	**0.10**	8.7		
FL8.23			62.6	37.8	0.60	21.0	0.00038	0.00004	0.00037	0.00004	2.46	0.25	7.53	0.15	**2.46**	**0.25**	8.8		

Table 2
Continued

Sample no.	Coordinates	Location	U ppm	Th ppm	Th/U	f206_8 %	$\frac{206Pb}{238U}$	±err	$\frac{208Pb}{232Th}$	±err	206/238 Age	±1s	208/232 Age	±1s	Best age Age (Ma)	±1s	εHf$_{(t)}$	δ^{18}O$_{SMOW}$	±
GAL140 (Beach sand)	S01°14′11.7″ W90°26′57.2″	Post-office																	
GAL140-1.1			477.1	409.1	0.86	5.6	0.00039	0.00000	0.00018	0.00000	2.55	0.03	3.55	0.13	*2.55*	*0.03*	9.3		
GAL140-2.1			423.0	542.5	1.28	53.2	0.00008	0.00000	0.00009	0.00000	0.54	0.02	1.80	0.02	*0.54*	*0.02*	8.8		
GAL140-3.1			422.3	595.2	1.41	61.4	0.00011	0.00000	0.00012	0.00001	0.69	0.02	2.48	0.17	*0.69*	*0.02*	10.7		
GAL140-4.1			400.9	535.2	1.34	30.4	0.00015	0.00000	0.00010	0.00000	0.96	0.01	2.13	0.03	*0.96*	*0.01*	10.5		
GAL140-5.1			182.7	103.2	0.56	6.0	0.00285	0.00004	0.00147	0.00008	18.37	0.25	29.78	1.57	*18.4*	*0.3*	6.7		
GAL140-6.1			627.1	773.6	1.23	28.9	0.00011	0.00000	0.00008	0.00000	0.69	0.02	1.67	0.06	*0.69*	*0.02*	10.9		
GAL140-7.1			392.3	395.7	1.01	19.4	0.00044	0.00001	0.00029	0.00001	2.85	0.05	5.82	0.12	*2.85*	*0.05*	8.6		
GAL149 (Beach sand)	S01°15′44.1″ W90°22′15.7″	Playa Las Cuevas																	
GAL149-1.1			205.0	115.6	0.56	60.3	0.00014	0.00000	0.00036	0.00000	0.93	0.03	7.30	0.03	*0.93*	*0.03*	11.5		
GAL149-2.1			498.9	505.3	1.01	72.7	0.00010	0.00000	0.00017	0.00001	0.68	0.02	3.37	0.11	*0.68*	*0.02*	10.8		
GAL149-4.1			945.9	852.5	0.90	44.1	0.00007	0.00000	0.00008	0.00001	0.46	0.02	1.65	0.11	*0.46*	*0.02*	8.8		
GAL149-5.1			1592.7	1663.9	1.04	15.8	0.00011	0.00000	0.00006	0.00000	0.72	0.01	1.30	0.03	*0.72*	*0.01*	10.0		
GAL149-7.1			640.6	494.0	0.77	28.6	0.00011	0.00000	0.00012	0.00000	0.69	0.01	2.38	0.07	*0.69*	*0.01*	7.9		
GAL149-10.1			180.1	120.2	0.67	29.7	0.00017	0.00000	0.00019	0.00001	1.09	0.03	3.95	0.19	*1.09*	*0.03*	10.9		
GAL149-11.1			325.8	473.2	1.45	28.6	0.00016	0.00000	0.00010	0.00000	1.02	0.03	2.10	0.09	*1.02*	*0.03*	10.4		
GAL149-12.1			210.5	211.7	1.01	74.5	0.00005	0.00001	0.00010	0.00000	0.31	0.03	1.98	0.05	*0.31*	*0.03*	7.3		
GAL149-13.1			830.9	990.3	1.19	5.0	0.00016	0.00001	0.00007	0.00000	1.06	0.03	1.33	0.08	*1.06*	*0.03*	10.6		
GAL149-14.1			563.0	741.2	1.32	6.1	0.00015	0.00001	0.00006	0.00000	0.94	0.03	1.20	0.07	*0.94*	*0.03*	11.4		
GAL149-15.1			598.3	299.7	0.50	31.5	0.00010	0.00000	0.00016	0.00004	0.63	0.03	3.23	0.86	*0.63*	*0.03*	11.2		
GAL149-16.1			87.8	49.5	0.56	11.9	0.00046	0.00002	0.00033	0.00002	2.96	0.11	6.64	0.34	*2.96*	*0.11*	8.3		
GAL172 (Beach sand)	S01°17′36.72″ W90°29′41.68″	south of la Loberia																	
GAL172-1.2			268.9	192.4	0.72	43.4	0.00029	0.00004	0.00042	0.00000	1.90	0.30	8.40	0.10	*1.90*	*0.30*	12.1		
GAL183 (Streambed deposit)	S01°15′44.1″ W90°22′15.7″	Stream at the Cueva de los piratas																	
GAL183-3.1			699.9	999.1	1.43	36.5	0.00034	0.00002	0.00025	0.00002	2.20	0.10	5.10	0.30	*2.20*	*0.10*	9.2		
San Cristobal																			

Table 2
Continued

Sample no.	Coordinates	Location	U ppm	Th ppm	Th/U	% f206_8	$\frac{206Pb}{238U}$	±err	$\frac{208Pb}{232Th}$	±err	206/238 Age	±1s	208/232 Age	±1s	Best age Age (Ma)	±1s	εHf(t)	δ18O SMOW	±
SCR2 (Beach sand)	S00°53'26.6" W89°36'43.53"	Cabo de Horno beach, Carola point																	
SCR-2.1			143.5	89.0	0.62	48.5	0.00011	0.00001	0.00021	0.00000	0.74	0.08	4.17	0.00	*0.74*	*0.08*	11.7		
SCR-2.2			285.9	183.3	0.64	26.1	0.00012	0.00001	0.00013	0.00002	0.79	0.04	2.69	0.36	*0.79*	*0.04*	13.1		
SCR-2.3			114.6	70.5	0.62	32.1	0.00023	0.00003	0.00030	0.00001	1.48	0.19	6.00	0.23	*1.48*	*0.19*	11.0		
SCR-2.4			35.3	23.4	0.66	70.4	0.00008	0.00006	0.00020	0.00015	0.52	0.41	4.02	2.93	*0.52*	*0.41*	11.3		
SCR-2.5			358.6	356.4	0.99	20.1	0.00012	0.00000	0.00008	0.00001	0.79	0.03	1.68	0.20	*0.79*	*0.03*	11.7		
SCR-2.6			217.1	133.4	0.61	20.5	0.00016	0.00002	0.00015	0.00001	1.02	0.12	3.09	0.17	*1.02*	*0.12*	11.5		
SCR-2.20			124.5	69.4	0.56	25.6	0.00033	0.00003	0.00039	0.00003	2.10	0.19	7.93	0.63	*2.10*	*0.19*	9.3		
SCR-2.24			301.5	128.0	0.42	5.1	0.00119	0.00004	0.00065	0.00005	7.68	0.26	13.15	1.04	*7.68*	*0.26*	6.4		
SCR2-2			288.7	171.4	0.59	3.8	0.00018	0.00001	0.00008	0.00000	1.18	0.07	1.67	0.09	*1.18*	*0.07*	8.7		
SCR2-3			476.7	288.8	0.61	16.9	0.00017	0.00001	0.00015	0.00000	1.11	0.05	2.99	0.01	*1.11*	*0.05*	10.5		
SCR2-4			256.1	174.2	0.68	13.4	0.00016	0.00003	0.00010	0.00001	1.03	0.18	2.13	0.12	*1.03*	*0.18*	10.3		
SCR2-7			137.1	111.9	0.82	12.7	0.00017	0.00001	0.00011	0.00001	1.12	0.06	2.13	0.22	*1.12*	*0.06*	9.6		
SCR2-10			334.4	367.7	1.10	0.6	0.00018	0.00000	0.00006	0.00000	1.19	0.02	1.25	0.03	*1.19*	*0.02*	9.1		
SCR2-11			521.5	479.6	0.92	2.0	0.00019	0.00002	0.00007	0.00001	1.25	0.17	1.41	0.12	*1.25*	*0.17*	11.5		
SCR2-12			689.5	1,172.6	1.70	45.0	0.00017	0.00002	0.00012	0.00000	1.13	0.15	2.50	0.10	*1.13*	*0.15*	6.1		
SCR2-13			50.6	28.1	0.55	29.2	0.00021	0.00002	0.00029	0.00000	1.38	0.16	5.80	0.04	*1.38*	*0.16*	11.6		
SCR2-14			124.2	48.2	0.39	35.6	0.00019	0.00002	0.00040	0.00001	1.22	0.15	8.03	0.29	*1.22*	*0.15*	9.3		
SCR2-16			152.8	123.1	0.81	71.6	0.00016	0.00003	0.00031	0.00000	1.03	0.19	6.26	0.06	*1.03*	*0.19*	10.6		
SCR3 (streambed deposit)	S00°55'32.5" W89°25'47.7"	Puerto Chino																	
SCR-3.2			886.6	1,514.4	1.71	2.6	0.00014	0.00001	0.00005	0.00000	0.92	0.03	1.00	0.03	*0.92*	*0.03*	12.6		
SCR-3.4			524.4	743.3	1.42	57.7	0.00014	0.00000	0.00014	0.00000	0.89	0.01	2.86	0.08	*0.89*	*0.01*	10.6		
SCR-3.8			102.2	56.7	0.6	0.57	0.00015	0.00004	0.00037	0.00003	0.94	0.23	7.50	0.67	*0.94*	*0.23*	13.3		
SCR-3.9			376.9	613.1	1.6	1.67	0.00011	0.00000	0.00005	0.00001	0.69	0.03	0.98	0.22	*0.69*	*0.03*	8.7		
SCR5 (Beach sand)	S00°55'30.09" W89°36'50.40"	La Loberia																	
SCR5-1			172.9	110.4	0.64	17.9	0.00015	0.00001	0.00013	0.00001	0.97	0.06	2.64	0.25	*0.97*	*0.06*	8.9		
SCR5-2			66.0	40.9	0.62	58.8	0.00014	0.00002	0.00030	0.00003	0.88	0.12	6.04	0.55	*0.88*	*0.12*	10.9		
SCR5-5			152.0	90.5	0.60	20.8	0.00015	0.00000	0.00016	0.00002	0.99	0.02	3.19	0.36	*0.99*	*0.02*	11.5		

Table 2
Continued

Sample no.	Coordinates	Location	U ppm	Th ppm	Th/U	% f206_8	206Pb/238U	±err	208Pb/232Th	±err	206/238 Age	±1s	208/232 Age	±1s	Best age Age (Ma)	±1s	εHf(t)	δ18O_SMOW ±
GAL40 (Basalt)	S00°54'29.60" W89°36'20.43"	N of Puerto Vaquerizo Moreno																
GAL40-1			2,044.2	3,644.3	1.78	26.1	0.00012	0.00000	0.00007	0.00001	0.8	0.0	1.4	0.1	*0.80*	*0.00*	8.5	
GAL40-2			1,605.2	9,524.4	5.93	−537.4	0.00012	0.00001	0.00002	0.00000	0.8	0.0	0.4	0.0	*0.80*	*0.00*	11.1	
GAL40-3			430.3	1,330.3	3.09	−14.2	0.00022	0.00002	0.00006	0.00000	1.4	0.1	1.2	0.0	*1.40*	*0.10*	9.9	
Isabela																		
Gal30 (Basalt with Palgioclase phenocryst)	S00°23'32.1" W90°59'44.0"	Volcán Alcedo																
GAL30-3.1			58.1	34.0	0.59	139.3	0.00003	0.00000	0.00019	0.00003	0.21	0.02	3.81	0.55	*0.21*	*0.02*	10.6	
GAL30-4.1			74.9	44.1	0.59	137.7	0.00002	0.00002	0.00017	0.00005	0.16	0.13	3.36	1.12	*0.16*	*0.13*	12.5	
GAL30-5.1			61.7	30.4	0.49	97.5	0.00002	0.00001	0.00011	0.00004	0.11	0.07	2.14	0.72	*0.11*	*0.07*	10.9	
GAL30-6.1			149.6	112.9	0.75	93.9	0.00002	0.00000	0.00008	0.00000	0.16	0.01	1.56	0.02	*0.16*	*0.01*	8.7	
GAL120 (Pumice)	S00°24'30.30" W90°59'13.30"	Volcan Alcedo, Punta Alfaro																
GAL120-2.1			61.2	44.1	0.72	96.6	0.00140	0.00012	0.06641	0.00146	9.04	0.75	1,299.53	27.63	*9.04*	*0.75*	8.8	
GAL120-4.1			265.9	236.2	0.89	98.4	0.00019	0.00001	0.00043	0.00001	1.22	0.10	8.63	0.17	*1.22*	*0.10*	9.7	
GAL122 (Beach sand)	S00°24'25.0"S W90°59'2.19"	Volcan north of Punta Alfaro																
GAL122-3.1			246.9	170.1	0.69	.	0.00000	0.00000	0.00003	0.00000	0.01	0.01	0.58	0.09	*0.01*	*0.01*	9.5	
GAL122-4.1			132.2	80.3	0.61	.	0.00001	0.00000	0.00009	0.00001	0.07	0.02	1.83	0.15	*0.07*	*0.02*	7.9	
GAL122-5.1			141.2	114.0	0.81	.	0.00001	0.00001	0.00003	0.00002	0.06	0.06	0.56	0.35	*0.06*	*0.06*	5.5	
GAL122-7.1			59.8	34.2	0.57	.	0.00000	0.00000	0.00007	0.00000	0.01	0.02	1.32	0.05	*0.01*	*0.02*	7.9	
GAL122-8.1			107.4	63.3	0.59	.	0.00001	0.00000	0.00005	0.00001	0.07	0.01	1.11	0.26	*0.07*	*0.01*	6.5	
GAL122-9.1			18.3	6.5	0.35	83.6	0.00002	0.00001	0.00013	0.00001	0.13	0.04	2.61	0.13	*0.13*	*0.04*	8.2	
GAL122-10.1			81.1	46.8	0.58	79.5	0.00002	0.00002	0.00008	0.00003	0.14	0.13	1.70	0.61	*0.14*	*0.13*	6.1	
Santa Fé																		
GAL43 (Beach sand)	S00°48'17.7" W90°05'09.3"	NE coast																
GAL43-1			38.3	16.5	0.43	16.3	0.00034	0.00007	0.00036	0.00014	2.20	0.42	7.25	2.86	*2.20*	*0.42*	7.5	
GAL43-2			36.8	14.3	0.39	27.9	0.00061	0.00014	0.00103	0.00027	3.93	0.89	20.83	5.52	*3.93*	*0.89*	9.8	

Table 2
Continued

Sample no.	Coordinates	Location	U ppm	Th ppm	Th/U	f206_8 %	206Pb/238U	±err	208Pb/232Th	±err	206/238 Age	±1s	208/232 Age	±1s	Best age (Ma) Age	±1s	εHf(t)	δ18O_SMOW	±
GAL45 (Basalt)																			
GAL45-1.1			254.5	204.3	0.80	5.3	0.00038	0.00002	0.00017	0.00001	2.44	0.11	3.41	0.25	*2.44*	*0.11*		7.5	
GAL47 (Beach sand)	S00°48'9.53" W90°02'26.93"	Barrington bay																	
GAL47-1			262.9	172.3	0.66	5.0	0.00035	0.00001	0.00016	0.00001	2.26	0.09	3.26	0.21	*2.26*	*0.09*		10.1	
GAL47-2			116.2	26.0	0.22	4.6	0.00040	0.00002	0.00030	0.00009	2.62	0.14	6.03	1.76	*2.62*	*0.14*		8.9	
GAL47-3			58.7	22.9	0.39	7.1	0.00040	0.00007	0.00027	0.00008	2.61	0.43	5.38	1.67	*2.61*	*0.43*		9.2	
GAL47-5			185.6	57.8	0.31	9.2	0.00035	0.00001	0.00032	0.00003	2.23	0.06	6.52	0.57	*2.23*	*0.06*		9.0	
GAL47-6			189.2	109.6	0.58	2.0	0.00034	0.00003	0.00013	0.00003	2.22	0.21	2.71	0.57	*2.22*	*0.21*		8.9	
GAL48 (Beach sand)	S00°48'13.9" W90°02'27.9"	Barrington bay																	
GAL48-1			65.0	23.4	0.36	−1.8	0.00028	0.00005	0.00006	0.00006	1.80	0.35	1.25	1.22	*1.80*	*0.35*		10.2	
GAL48-2			93.4	46.4	0.50	5.5	0.00033	0.00001	0.00018	0.00011	2.12	0.04	3.57	2.23	*2.12*	*0.04*		9.0	
GAL48-3			207.2	119.4	0.58	5.0	0.00032	0.00001	0.00016	0.00002	2.07	0.05	3.22	0.40	*2.07*	*0.05*		9.4	
GAL48-4			32.5	12.9	0.40	14.1	0.00025	0.00002	0.00026	0.00003	1.60	0.12	5.20	0.55	*1.60*	*0.12*		9.3	
GAL48-5			151.9	88.6	0.58	5.2	0.00031	0.00003	0.00016	0.00002	2.02	0.23	3.16	0.40	*2.02*	*0.23*		9.8	
GAL48-6			39.8	20.1	0.51	19.8	0.00040	0.00005	0.00043	0.00013	2.56	0.35	8.63	2.58	*2.56*	*0.35*		8.3	
Rábida																			
GAL28 (Beach sand)	S00°24'14.8" W90°42'11.2"																		
GAL28-1			180.1	131.0	0.73	11.2	0.00012	0.00003	0.00007	0.00000	0.80	0.19	1.45	0.05	*0.80*	*0.19*		10.0	
GAL28-2			86.7	58.0	0.67	3.3	0.00012	0.00003	0.00007	0.00000	0.80	0.19	1.45	0.05	*0.80*	*0.19*		9.1	
GAL28-3			102.6	66.1	0.64	−0.5	0.00016	0.00002	0.00005	0.00003	1.04	0.14	1.00	0.59	*1.04*	*0.14*		10.5	
GAL28-4			91.7	37.2	0.41	22.9	0.00008	0.00004	0.00011	0.00002	0.50	0.28	2.19	0.32	*0.50*	*0.28*		9.1	
GAL28-5			573.3	938.7	1.64	−8.6	0.00014	0.00000	0.00003	0.00000	0.91	0.01	0.67	0.06	*0.91*	*0.01*		11.6	
GAL29 (Basalt)	S00°24'14.8" W90°42'11.4"																		
GAL29B-1.1			97.6	64.5	0.66	107.0	0.00013	0.00000	0.00046	0.00001	0.82	0.01	9.30	0.29	*0.82*	*0.01*		9.6	
GAL29B-2.1			68.2	39.9	0.59	131.3	0.00013	0.00002	0.00061	0.00001	0.88	0.15	12.38	0.19	*0.88*	*0.15*		9.6	
GAL29B-3.1			104.4	58.6	0.56	102.1	0.00017	0.00001	0.00067	0.00003	1.09	0.06	13.53	0.57	*1.09*	*0.06*		10.3	
GAL29B-4.1			142.6	108.6	0.76	121.5	0.00013	0.00001	0.00044	0.00001	0.83	0.04	8.89	0.12	*0.83*	*0.04*		10.6	
GAL29B-5.1			223.7	293.3	1.31	76.9	0.00015	0.00001	0.00020	0.00001	0.95	0.10	4.07	0.25	*0.95*	*0.10*		8.7	
GAL29B-6.1			114.2	79.4	0.70	18.3	0.00013	0.00001	0.00012	0.00000	0.87	0.06	2.35	0.06	*0.87*	*0.06*		8.3	
GAL29B-7.1			124.1	93.9	0.76	21.4	0.00013	0.00001	0.00012	0.00001	0.86	0.05	2.43	0.12	*0.86*	*0.05*		8.9	

Table 2
Continued

Sample no.	Coordinates	Location	U ppm	Th ppm	Th/U	% f206_8	$\frac{206Pb}{238U}$	±err	$\frac{208Pb}{232Th}$	±err	206/238 Age	±1s	208/232 Age	±1s	Best age Age (Ma)	±1s	$\varepsilon Hf_{(t)}$	$\delta^{18}O_{SMOW}$	±
GAL29B-8.1			205.1	235.9	1.15	14.5	0.00012	0.00001	0.00006	0.00000	0.77	0.05	1.31	0.08	*0.77*	*0.05*	9.1		
GAL29B-9.1			237.2	236.0	0.99	9.9	0.00016	0.00001	0.00008	0.00001	1.01	0.05	1.52	0.14	*1.01*	*0.05*	6.9		
GAL29B-10.1			169.5	139.4	0.82	14.0	0.00014	0.00001	0.00009	0.00002	0.91	0.07	1.78	0.40	*0.91*	*0.07*	9.1		
GAL29B-11.1			134.8	109.0	0.81	13.6	0.00013	0.00001	0.00009	0.00000	0.87	0.04	1.89	0.09	*0.87*	*0.04*	9.7		
GAL29B-12.1			137.6	145.5	1.06	58.8	0.00015	0.00001	0.00021	0.00000	0.96	0.04	4.20	0.03	*0.96*	*0.04*	8.3		
Española																			
GAL53 (Beach sand)	S01°21'15.32" W89°39'34.64"	Gardner bay																	
GAL53-2			2,659.4	3,708.1	1.39	10.1	0.00053	0.00001	0.00024	0.00002	3.44	0.07	4.76	0.42	*3.44*	*0.07*	8.5		
GAL53-1.1			377.6	396.5	1.05	15.9	0.00028	0.00001	0.00016	0.00000	1.82	0.03	3.29	0.08	*1.82*	*0.03*	13.6		
GAL53-2.1			316.9	244.0	0.77	26.7	0.00030	0.00001	0.00029	0.00002	1.93	0.05	5.76	0.31	*1.93*	*0.05*	10.9		
GAL53-3.1			333.9	295.9	0.89	1.9	0.00032	0.00002	0.00011	0.00000	2.06	0.10	2.32	0.07	*2.06*	*0.10*	13.2		
GAL53-4.1			327.9	193.1	0.59	3.3	0.00036	0.00001	0.00015	0.00001	2.31	0.09	3.00	0.27	*2.31*	*0.09*	11.6		
GAL53-5.1			530.5	456.9	0.86	6.0	0.00030	0.00001	0.00014	0.00001	1.97	0.09	2.81	0.13	*1.97*	*0.09*	11.0		
GAL53-6.1			711.1	944.0	1.33	7.0	0.00008	0.00000	0.00003	0.00000	0.50	0.02	0.67	0.04	*0.50*	*0.02*	9.9		

Note. $\varepsilon Hf_{(t)}$ and $\delta^{18}O$ data are also included in bold italic best age.

Table 3
SHRIMP II Analytical Data for Spot Analyses of Zircon Grains Older Than the Galápagos Plume Array (GPA) Zircons (>164 Ma) in Bold Italic Best Age

Sample No.	Coordinates	Location	U ppm	Th ppm	Th/U	206Pb/204Pb	207Pb/206Pb	206Pb/238U	207Pb/235U	206/238 Age ± 1s	207/235 Age ± 1s	207/206 Age ± 1s	Best age Age (Ma)	±1s	εHf(t)	δ18O SMOW	±
Santa Cruz																	
GAL3 (Beach sand)	S00°45′49.56″ W090°20′25.14″	Tortuga Bay (Playa mansa)															
GAL3-1			312	169	0.54	39,667	0.0575 ± 6	0.0812 ± 7	0.644 ± 10	503 ± 4	505 ± 6	513 ± 23	*503*	*4*	4.1	9	0.1
GALl3-2			322	184	0.57	1,329	0.2039 ± 6	0.5571 ± 51	15.67 ± 16	2,855 ± 21	2,857 ± 10	2,858 ± 5	*2,858*	*5*	−8.8	8	0.1
GAL3-3			436	220	0.50	62,617	0.2304 ± 2	0.6031 ± 55	19.16 ± 18	3,042 ± 22	3,050 ± 9	3,055 ± 2	*3,055*	*2*	−11.3	5	0.1
GAL3-4			453	50	0.11	180,180	0.0669 ± 3	0.1393 ± 13	1.286 ± 13	841 ± 7	839 ± 6	836 ± 8	*841*	*7*	−8.5	11	0.1
GAL3-5			74	63	0.85	20,907	0.0575 ± 14	0.0816 ± 8	0.647 ± 18	506 ± 4	507 ± 11	513 ± 54	*506*	*4*	−11.5	8.7	0.1
GAL3-6			165	80	0.48	42,827	0.1961 ± 4	0.5487 ± 51	14.834 ± 14	2,820 ± 21	2,805 ± 9	2,794 ± 3	*2,794*	*3*	−3.5	6.00	0.10
GAL6 (lava tube deposit)	S00°39′34.8″ W090°16′09.3″	Cueva Cascajo															
GAL6-1			191	57	0.30	149,254	0.0931 ± 4	0.2585 ± 24	3.32 ± 4	1,482 ± 12	1,485 ± 8	1,489 ± 8	*1,489*	*8*	4.4	8.40	0.10
GAL6-2			33	8	0.24	37,807	0.0487 ± 37	0.0034 ± 1	0.023 ± 2	22 ± 1	23 ± 2	132 ± 150	*22.0*	*1.0*	11.4	4.95	0.07
GAL6-3			493	183	0.37	203,252	00.750 ± 2	0.1784 ± 16	1.85 ± 2	1,058 ± 9	1,062 ± 7	1,069 ± 6	*1,058*	*9*	−5.8	11.3	0.1
GAL6-7			115	79	0.69	32,852	0.0464 ± 15	0.0085 ± 1	0.055 ± 2	55 ± 1	54 ± 2	20 ± 47	*55.0*	*1.0*	8.0	7.13	0.04
GAL6-8			93	80	0.86	19,301	0.0556 ± 15	0.604 ± 6	0.463 ± 14	378 ± 3	386 ± 10	435 ± 61	*378*	*3*	−5.1	8.20	**0.10**
GAL6-11			728	161	0.22	209,644	0.0603 ± 2	0.0997 ± 9	0.828 ± 8	613 ± 5	613 ± 5	613 ± 8	*613*	*5*	−6.1	7.20	0.10
GAL6-14			90	22	0.24	18,015	0.0668 ± 10	0.1383 ± 13	1.28 ± 2	835 ± 7	835 ± 10	833 ± 30	*835*	*7*	6.7	5.63	0.10
Baltra																	
Gal86 (Beach sand)	S00°28′26.2″ W90°15′40.8″	SE of Baltra Island at canal Itabaca															
Gal86-1			217	145	0.67	5,956	0.0246 ± 946	0.0146 ± 14	0.049 ± 191	93 ± 9	43 ± 109	0 ± 972	*93.0*	*9.0*	9.0		
Gal86-3.1			244	141	0.58	1,843	0.0438 ± 186	0.0146 ± 3	0.088 ± 38	94 ± 2	86 ± 35	0 ± 345	*94.0*	*2.0*	10.8		
Gal86-3.2 (rim)			109	72	0.66	786	0.1579 ± 3,432	0.0026 ± 9	0.056 ± 120	18 ± 0.3	0 ± 32	0 ± 1,350	*18.5*	*0.3*	1.7		
Gal86-4.2 (core)			253	186	0.73	187.8	0.0788 ± 1,251	0.0033 ± 4	0.036 ± 58	21 ± 3	36 ± 46	1,166 ± 1,429	*21.0*	*3.0*	2.4		
Pinzón																	
GAL36 (Basalt)	S00°36′10.0″ W90°38′54.7″	Western coast															
GAL36-1			742	276	0.37	7,268	0.0530 ± 3	0.0518 ± 6	0.378 ± 5	326 ± 4	326 ± 4	329 ± 13	*326*	*4*	−7.9		

Table 3
Continued

Sample No.	Coordinates	Location	U ppm	Th ppm	Th/U	206Pb/204Pb	207Pb/206Pb	206Pb/238U	207Pb/235U	206/238 Age ± 1s	207/235 Age ± 1s	207/206 Age ± 1s	Best age Age (Ma)	±1s	$\varepsilon Hf_{(t)}$	$\delta^{18}O_{SMOW}$	±
Genovesa																	
GAL54 (Beach sand)	N00°19′6.42″ W89°56′57.81″	Bahia Genovesa															
GAL54-1			925	145	0.16	132,275	0.0593 ± 2	0.0933 ± 8	0.763 ± 8	575 ± 5	576 ± 4	578 ± 8	575	5	−8.1	7.83	0.10
GAL54-2			94	65	0.69	302,115	0.1005 ± 3	0.3029 ± 27	4.20 ± 4	1,706 ± 13	1,674 ± 8	1,634 ± 6	1,634	6	3.3		
Floreana																	
FL6 (Beach sand)	S01°16′34.6″ W90°29′17.4″	Playa Negra															
FL6.3			302	77	0.25	79,808	0.0743 ± 3	0.1776 ± 17	1.819 ± 20	1,054 ± 9	1,052 ± 7	1,049 ± 8	1,054	9	4.1		
FL8 (Beach sand)	S01°15′44.1″ W90°22′15.7″	Las Cuevas beach															
FL8-1			105	209	1.99	10,405	0.0582 ± 22	0.0952 ± 9	0.764 ± 30	586 ± 5	576 ± 17	539 ± 82	586	5	−24.9	5.79	0.11
FL8-5			156	151	0.97	75,758	0.0684 ± 6	0.1459 ± 13	1.377 ± 18	878 ± 8	879 ± 8	881 ± 18	878	8	1.8	4.68	0.07
GAL70 (Beach sand)	S01°16′34.4″ W90°29′17.2″	Playa Negra															
GAL70-1.1			149	88	0.59	1,490	0.0520 ± 72	0.0250 ± 3	0.180 ± 25	159 ± 2	168 ± 22	287 ± 288	159	2	4.7		
GAL70-2.1			980	851	0.87	1,514	0.0485 ± 26	0.0258 ± 2	0.172 ± 10	164 ± 1	161 ± 8	123 ± 123	164	1	6.0		
GAL147 (Beach sand)	b	Playa de tortugas, punta Cormorán															
GAL147-1			130	82	0.63	13,387	0.0848 ± 30	0.2263 ± 19	2.65 ± 10	1,315 ± 10	1,314 ± 28	1,312 ± 28	1,312	28	0.9		
GAL149 (Beach sand)	S01°15′44.1″ W90°22′15.7″	Playa Las Cuevas															
Gal149-6.1			197	111	0.56	758	0.0406 ± 228	0.0082 ± 1	0.046 ± 24	53 ± 1	46 ± 13	0 ± 152	53.0	1.0	9.8		
GAL149-8			188	60	0.32	3,755	0.0476 ± 91	0.0366 ± 4	0.240 ± 46	232 ± 3	218 ± 38	77 ± 239	232	3	−2.1		
GAL149-17 (core)			696	513	0.74	19,794	0.1660 ± 1	0.4720 ± 59	10.80 ± 14	2,492 ± 26	2,506 ± 12	2,517 ± 1	2,517	1	1.0		
GAL149-18 (rim)			124	122	0.98	195,313	0.1655 ± 2	0.4375 ± 55	9.99 ± 13	2,339 ± 25	2,433 ± 12	2,513 ± 2	2,513	2	−0.6		
GAL 155 (Beach sand)	S01°15′58.38″ W90°29′15.10″	north of Puerto Velazco															
GAL155-1.1			236	69	0.29	49,237	0.0799 ± 7	0.2038 ± 13	2.243 ± 27	1,195 ± 7	1,195 ± 8	1,194 ± 18	1,195	8	7.4		
GAL155-2.1			3,480	959	0.28	48,426	0.0522 ± 3	0.0496 ± 3	0.357 ± 3	312 ± 2	310 ± 2	294 ± 14	312	2			

Table 3
Continued

Sample No.	Coordinates	Location	U ppm	Th ppm	Th/U	206Pb/204Pb	207Pb/206Pb	206Pb/238U	207Pb/235U	206/238 Age ± 1s	207/235 Age ± 1s	207/206 Age ± 1s	Best age Age (Ma)	±1s	εHf$_{(t)}$	δ^{18}O$_{SMOW}$	±
GAL155-3.1			310	66	0.21	8,033	0.0720 ± 9	0.1654 ± 11	1.642 ± 24	986 ± 6	986 ± 9	986 ± 25	*986*	*6*			
GAL155-4.1 (core)			994	52	0.05	5,814	0.0587 ± 8	0.0899 ± 6	0.727 ± 11	555 ± 3	555 ± 7	555 ± 29	*555*	*3*	−27.7		
GAL155-4.2 (rim)			476	37	0.08	3,040	0.0511 ± 26	0.0336 ± 2	0.237 ± 12	213 ± 1	216 ± 10	247 ± 115	*213*	*1*	−3.7		
GAL155-5.1			427	104	0.24	188	0.0607 ± 40	0.0021 ± 1	0.018 ± 12	14 ± 1	18 ± 12	629 ± 821	*14.0*	*1.0*	10.1		
GAL155-6.1			411	317	0.77	36,873	0.0787 ± 5	0.2042 ± 13	2.215 ± 22	1,198 ± 7	1,186 ± 7	1,164 ± 13	*1,186*	*7*	3.8		
GAL155-7.1			200	120	0.60	6,859	0.0591 ± 18	0.0879 ± 6	0.717 ± 22	543 ± 3	549 ± 13	572 ± 65	*543*	*3*	−7.6		
GAL160 (Beach sand)	S01°17′6.07″ W90°29′38.07″	Beach sand south of la Loberia															
GAL160-1			6,344	1,628	0.26	50,891	0.0546 ± 2	0.0640 ± 4	0.482 ± 4	400 ± 2	400 ± 3	398 ± 9	*400*	*2*			
GAL162 (Basalt)	S1°17′21.42″ W90°29′45.71″	south of la Loberia															
GAL162-1.1			259	105	0.41	14,959	0.0752 ± 11	0.1787 ± 12	1.853 ± 31	1,060 ± 6	1,064 ± 11	1,074 ± 29	*1,060*	*6*	8.2		
GAL162-1.2			95	41	0.43	1,726	0.0733 ± 35	0.1687 ± 13	1.706 ± 85	1,005 ± 7	1,011 ± 32	1,023 ± 98	*1,005*	*7*	7.1		
GAL162-2.1			255	113	0.44	18,044	0.0791 ± 9	0.1991 ± 13	2.171 ± 29	1,171 ± 7	1,172 ± 9	1,174 ± 21	*1,172*	*9*	6.1		
GAL162-3.1			226	145	0.64	8,619	0.0734 ± 10	0.1691 ± 11	1.711 ± 27	1,007 ± 6	1,013 ± 10	1,025 ± 27	*1,007*	*6*	−5.9		
GAL172 (Beach sand)	S01°17′36.72″ W90°29′41.68″	south of la Loberia															
GAL172-1.1			53	44	0.83	2,253	0.1240 ± 26	0.3586 ± 31	6.301 ± 150	2,023 ± 15	2,019 ± 21	2,014 ± 37	*2,014*	*37*	−9.1		
GAL197 (streambed deposit)	S01°15′40.23″ W90°26′07.28″	Stream coming down Cerro Ventana to Post Office															
GAL197-1.1			268	266	1.00	20,829	0.0856 ± 7	0.2291 ± 15	2.703 ± 31	1,330 ± 8	1,329 ± 8	1,328 ± 17	*1,329*	*8*	2.8		
GAL197-1.2			200	140	0.70	54,377	0.0857 ± 11	0.2313 ± 15	2.735 ± 41	1,341 ± 8	1,338 ± 11	1,332 ± 24	*1,338*	*11*	2.6		
GAL197-2.1			970	460	0.47	1,237	0.0537 ± 17	0.0611 ± 4	0.453 ± 15	382 ± 2	379 ± 10	360 ± 71	*382*	*2*	−5.0		
GAL197-3.1			376	137	0.36	67,159	0.0965 ± 5	0.2735 ± 18	3.636 ± 33	1,558 ± 9	1,557 ± 7	1,556 ± 11	*1,557*	*7*	2.2		
GAL197-4.1			229	100	0.44	7,013	0.0740 ± 9	0.1747 ± 11	1.783 ± 27	1,038 ± 6	1,039 ± 10	1,042 ± 25	*1,038*	*6*	2.0		
GAL197-5.1			238	241	1.01	12,101	0.0582 ± 19	0.0939 ± 6	0.754 ± 26	578 ± 4	570 ± 15	538 ± 72	*578*	*4*	−17.5		

Table 3
Continued

Sample No.	Coordinates	Location	U ppm	Th ppm	Th/U	$\frac{206Pb}{204Pb}$	$\frac{207Pb}{206Pb}$	$\frac{206Pb}{238U}$	$\frac{207Pb}{235U}$	$\frac{206/238}{Age \pm 1s}$	$\frac{207/235}{Age \pm 1s}$	$\frac{207/206}{Age \pm 1s}$	Best age Age (Ma)	±1s	$\varepsilon Hf_{(t)}$	$\delta^{18}O_{SMOW}$	±
GAL197-6.1			255	350	1.37	6,169	0.0640 ± 16	0.1262 ± 8	1.114 ± 29	766 ± 5	760 ± 14	742 ± 51	*766*	*5*	−9.5		
GAL197-7.1			396	422	1.06	944	0.0535 ± 28	0.0566 ± 4	0.417 ± 22	355 ± 2	354 ± 16	351 ± 119	*355*	*2*	−2.8		
GAL197-8.1			1,589	531	0.33	17,173	0.0531 ± 5	0.0613 ± 4	0.449 ± 55	384 ± 2	376 ± 4	333 ± 22	*384*	*2*	−1.0		
San Cristobal																	
SCR3 (streambed deposit)	S00°55′32.5″ W89°25′47.7″	Puerto Chino															
SCR3-3			503	205	0.41	93,809	0.0947 ± 5	0.2658 ± 35	3.47 ± 5	1,519 ± 18	1,521 ± 11	1,522 ± 9	*1,522*	*9*	−0.5		
Isabela																	
Gal30 (Basalt with Palgioclase phenocryst)	S00°23′32.1″ W90°59′44.0″	Volcán Alcedo															
GAL30-1			212	99	0.47	29,586	0.0585 ± 28	0.0258 ± 3	0.209 ± 85	164 ± 2	177 ± 9	356 ± 112	*164*	*2*	9.7		
Santa Fé																	
al230 (Beach sand)	S00°49′34.22″ W90°01′45.37″	Punta del miedo															
Gal230-1.1			29	12	0.41	44.6	0.6034 ± 253	0.0101 ± 25	0.838 ± 428	65 ± 6	618 ± 241	4,516 ± 1,854	*65.0*	*6.0*	13		

The results of this study are displayed in Figure 10 and show that, except for one grain (with a 21.0 Ma core and a 18.5 Ma rim; Figures 5 and 6), all zircon grains with ages up to 164 Ma exhibit high positive $\varepsilon Hf_{(t)}$ (6–14; Tables S1 and S2) and $\delta^{18}O_{(zircon)}$ values well within the range of mantle zircon (Valley et al., 2005) (4–6‰; Table S4 in Supporting Information S1). The zircon grains within this ∼0–164 Ma range are distributed continuously without significant age gaps, defining a "Galápagos plume array" (GPA; Figure 10a). Zircon younger than 0.2 Ma (steep slope in Figure 10b) is not as abundant as zircons in the range 0.2–4 Ma (shallow slope in Figure 10b). This is consistent with the arid climate and the resulting lack of fluvial erosion throughout most of the archipelago which have prevented significant erosion of the youngest subaerial lavas (Geist et al., 2014). GPA zircon that has pre-Galápagos Archipelago ages in the range ∼4–164 Ma is scarce (steep slope in Figure 10b) but spreads evenly and is isotopically indistinguishable from the younger <4 Ma zircon, suggesting the same plume-related mantle origin. This is consistent with existing isotopic data of whole rocks, olivine and plagioclase from the Archipelago and associated Carnegie, Cocos, Malpelo and Coiba ridges (Figure 10a), reinforcing the view that GPA zircons crystalized from plume-related liquids.

The GPA trend is interrupted at 164 Ma (Figure 10a) by the appearance of low $\varepsilon Hf_{(t)}$ and high $\delta^{18}O_{(zircon)}$ values in zircon of Triassic (213 Ma) and older age (non-GPA). The grains show variable textures and sizes (all larger than 100 μm), mostly broken and with rounded terminations (Figure 7). CL images often reveal core-rim features, some with oscillatory zoned cores surrounded by recrystallized or newly grown rims too thin to be measure by the SHRIMP spot. The non-GPA zircon forms a distinct array extending in ages from 213 to 3,055 Ma with heterogenous $\varepsilon Hf_{(t)}$ and $\delta^{18}O_{(zircon)}$. Whereas zircon in the range ∼213–835 Ma (plus an outlier zircon grain with a 21.0 Ma core and a 18.5 Ma rim) shows mostly low $\varepsilon Hf_{(t)}$ (−27.7 to 1.8, only two show higher values at 4.1 and 6.7) and generally high $\delta^{18}O_{(zircon)}$ (4.7–10.8‰), typical of continental crust, zircon in the range ∼835–3,055 Ma has a variety of $\varepsilon Hf_{(t)}$ (−9.1 to 8.2) and $\delta^{18}O_{(zircon)}$ (4.7–11.3‰) values consistent with both juvenile and continental crust signatures.

3.1. 2D/3D Thermo-Mechanical Numerical Simulations of Plume-Lithosphere Interaction

The results of our thermo-mechanical numerical simulations show that after an initial rising stage, the plume head is sheared along with the moving plate, and splits into smaller plumes that produce partial melt beneath the lithosphere (Figure 8a). Zircons crystallized in these partially molten regions (e.g., GPA zircons ∼164 Ma), are colored green or violet (depending on whether they formed from plume or ambient mantle material) to track their subsequent location. We initially introduce 90,000 passive tracers that represent zircon. The tracers are placed in the upper mantle and we track their motion once the surrounding mantle partially melts for the first time, as a proxy for zircons that formed but did not immediately erupt. Their subsequent path is tracked until they arrive in a partially molten region for the second time, when they are assumed to be extracted to the surface along with freshly erupting lavas. In the simulations, the zircon age is accordingly the age between formation and eruption (in Myrs). Zircon that is transported to depths >300 km has its U-Pb age reset upon reidite formation (Rasmussen et al., 2020) and is no longer considered in the interpretation.

The model results show that zircon can stay in the shallow upper mantle for extended periods of time (Figure 8 and Movie S1). Perhaps counterintuitively, not all zircon is dragged along with the moving lithosphere, but much instead initially moves in the opposite direction. This is because the plume's rising velocity is larger than the plate motion, which induces small scale convective cells (Figures 8b and 8c). Some of this zircon returns to the plume region, whilst the rest is mixed in with the asthenospheric upper mantle. The dynamics of the plume is cyclic, with periods of slow and steady activity interrupted by more active phases. This results in discontinuous magmatic activity and sub-lithospheric circulation patterns that are mostly confined to the uppermost asthenospheric mantle, allowing the preservation of zircons. Most passive tracers are erupted to the surface within 50 million years of plume formation and contain relatively young zircons (Figures 8d and 8e). Yet, old zircons can be dragged into these lavas and erupt as well, in accordance with our observations in the Galápagos Archipelago. It should be noted that our simulations only track old zircons and that it takes some time for the initial plume to arrive at the lithosphere-asthenosphere boundary and produce melt. Accordingly, the youngest zircons in the simulations are ∼10 Ma (Figure 8d). Yet, qualitatively the shape of the curve is remarkably similar to our data from Galapagos (see also Figure S9 in Supporting Information S1).

In order to test the sensitivity of our results to changes in the model parameters, we performed systematic simulations that demonstrate that the features described above are robust. The analysis shows that some differences
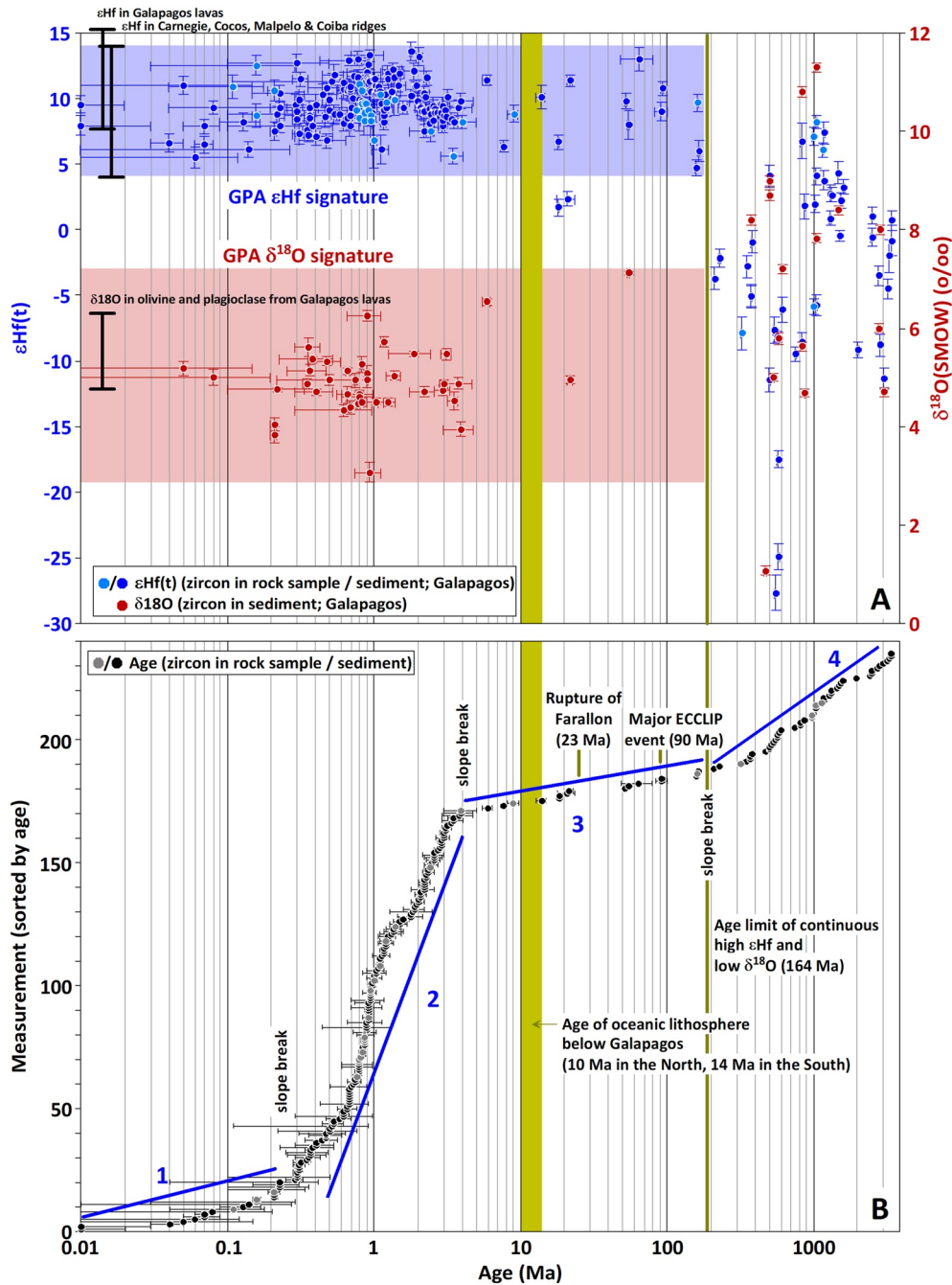
Figure 10. Isotopic composition ($\varepsilon Hf_{(t)}$ and $\delta^{18}O_{(zircon)}$) and age of Galápagos zircons. (a) U-Pb age versus $\varepsilon Hf_{(t)}$ (blue) and $\delta^{18}O_{(zircon)}$ (red) of analyzed zircons. Both high $\varepsilon Hf_{(t)}$ and low $\delta^{18}O_{(zircon)}$ define the Galápagos Plume Array (GPA, blue and red rectangles, respectively), which extends from 0 Ma to ca. 170 Ma (note significant scatter at >170 Ma). A similar isotopic composition in the range of the GPA is shown in black bars which represent the ranges of εHf in Galapagos lavas and Carnegie, Cocos, Malpelo and Coiba ridges and the Caribbean Large Igneous Province, respectively, and for $\delta^{18}O$ in olivine and plagioclase from Galapagos lavas and xenoliths (Blichert-Toft & White, 2001; (d) Geist et al., 1998; Geldmacher et al., 2003; Peterson et al., 2019). The data can be found in Supporting Table S8. (b) Age of analyzed zircons sorted by age of spot. The distribution shows four sectors separated by slope breaks, including 1: age range of zircon of less eroded (most recent) volcanic rocks (<0.2 Ma); 2: age range of zircon of most abundant volcanic rocks exposed to erosion (0.2–4 Ma); 3 and 4: age ranges of pre-Galápagos Islands zircon, comprising 3: zircons belonging to the GPA that extend from 4 to 164 Ma well beyond the oldest age of the exposed lavas and the age of basement oceanic lithosphere (10–14 Ma), and 4: exotic zircons older than 164 Ma with scattered $\varepsilon Hf_{(t)}$ and $\delta^{18}O$, including continental crust signature. For reference, 23 Ma (estimated split of Farallon plate) and 90 Ma (major Ecuadorian-Colombian-Caribbean-Large-Igneous-Province event) are indicated in (b). In A and B, lighter colored circles for $\varepsilon Hf_{(t)}$ and age data, respectively, correspond to zircon grains separated from rock samples.

in the model results arise as a function of plume radius, temperature and age of oceanic plate. Old oceanic plates (40 Ma) reduce the amount of melt produced, but can preserve very old zircons (~130 Ma), while young plates (15 Ma) generally give rise to a smaller amount of old zircons (see Figures S3–S5 in Supporting Information S1). A smaller plume radius (<100 km) produces less melt, while higher plume temperatures result in a molten layer below the lithosphere with corresponding young zircon ages. Plate velocity, lateral boundary conditions, the manner in which the plume is introduced in the models, as well as 2D versus 3D effects are all of second order importance (Figures S6–S11 in Supporting Information S1).

4. Discussion

4.1. Potential Sources of the Non-GPA Zircons

The non-GPA zircon grains indicate old (>213 Ma) to recent (~20 Ma, for the outlier) external sources not related to plume activity. Galápagos is situated on very young oceanic lithosphere and unlike Mauritius and Iceland, where rare old continental zircon has also been found (Ashwal et al., 2017; Torsvik et al., 2015), seismic studies preclude the presence of fragments of continental crust beneath the Galápagos Archipelago (Villagómez et al., 2014). Unlike the old zircons and suspected Archean fragments found in the mid-Atlantic region (Bea et al., 2020; Bortnikov et al., 2008, 2019; Pilot et al., 1998; Skolotnev et al., 2010), the Pacific has no recent history of continental rifting. The Pacific mantle domain developed from the breakup of the Neoproterozoic and penultimate supercontinent Rodinia after ~700 Ma (Palaeo-Pacific Ocean or the later Panthalassan superocean) (Cawood, 2005). Due to the switch of subduction polarity, from that directed toward the future Pacific domain to that directed away the Pacific, soon after the breakup of the supercontinent Rodinia (~600 Ma), little continental material has been recycled into the Pacific mantle domain. Thus, subduction polarity associated with the supercontinent cycle and super ocean evolution could probably explain why the Pacific mantle domain has been protected from contamination with continental crustal materials for much of the past 600 Myr. Alternatively it is possible that some continental blocks/slivers stay stranded forever in Pacific mantle (invisible to seismic studies (Villagómez et al., 2014)) owing to the same mechanism as in the Southwest Indian Ridge (Liu et al., 2022).

Nevertheless, the source of these exotic non-GPA zircons is enigmatic and may include a combination of processes, such as (a) Anthropogenic contamination, (b) Contamination of sands by bird dropping, (c) Strong trans-oceanic atmospheric dust clouds from the continent, (d) Subaqueous transport by ocean currents, (e) Far-traveled volcanic pumice, (f) Volcanic super-eruptions, (g) Magmatic assimilation of detrital oceanic sediments, (h) Contamination of the asthenosphere by subducted material. We now discuss in detail each of the processes.

4.1.1. Anthropogenic Contamination

Three sources of possible anthropogenic contamination can be considered, (a) building material brought from the continent to build residential environments, (b) tourism, (c) laboratory contamination (for more detail see analytical procedure). According to the website of Galapagos conservation (https://galapagosconservation.org.uk/projects/sustainable-buildings-project/), the majority of houses built in Galapagos are made with concrete breeze blocks from materials often sourced from two local mines located within the Galapagos National Park. Blocks made from alternative aggregates such as broken glass are made in Galapagos by artisanal manufacturers; however, by far the most-sustainable building material available in the Islands is bamboo. In any case, considering the possibility that some constructions may have been made with material brought from the mainland, it should be noted that these residences are only located in San Cristobal, Floreana, Santa Cruz and Isabela, far from the locations where the detrital samples were taken (except for Playa Negra in Floreana (GAL70, FL6; Figure 2)). In addition, another consideration regarding the building material brought from the mainland as a possible source of contamination is that this material must contain zircons. This is unlikely as the material is produced by heating limestone and clay or other silicate mixtures (which do not contain zircon) to very high temperatures.

Over 200,000 tourists visit Galapagos each year (Apolo et al., 2019), the majority through Baltra, north of Santa Cruz, and less through San Cristobal (Figure 2). It is theoretically possible that zircon grains can be brought into the islands in the shoes/boots and other clothing material of tourists, but it is rather unlikely that these zircon grains will survive on the soles of the shoes to get to other islands, particularly given the precautions of the parc which does not allow the use of the same shoes at different islands.

4.1.2. Contamination of Sands by Bird Dropping

The number of regular migrant birds in the Galapagos islands total 27 species (Wiedenfeld, 2006). The vast majority of them (23) are coast and lagoon/marine birds whose diet consist mostly of fish, shrimps, insects, crustaceans, mollusks, worms, etc. These species do not deliberately ingest soil, but rather would do it only accidently by searching for food on beach sands and mud. Birds that ingest sand to gravel-sized particles to help their digestive process (geophagy) are mostly land birds; therefore, it is unlikely that sea birds will transport zircons from the south American continent to Galapagos (Downs et al., 2019). Additionally, such a process cannot explain the overwhelming abundance of zircons younger than 4 Ma. It would mean that the birds selectively eat sediments derived from young juvenile rocks, a rather unexpected process if we take into account the variety of soils formed in South America and the Andes.

4.1.3. Strong Trans-Oceanic Atmospheric Dust Clouds From the Continent

Owing to gravitational settling, dust particle size decreases with increasing distance from the source (Holz et al., 2004; Mahowald et al., 2014; Sarnthein et al., 1981; Schütz, 1980) and generally do not exceed 20 µm when transported over long distances (Gillette, 1979; Tsoar & Pye, 1987). The zircons found and dated in Galapagos are all in the range from ∼80 to 300 µm with some bigger grains of more than 1 mm. On the other hand, according to Aarons et al. (2013), transport models with variable dust particle diameter and wind speed demonstrate the preferential depletion of zircon during transport of dust from the source area. Inputs of African dust are more important to the genesis of soils on islands in the western Atlantic Ocean than previously supposed (Muhs et al., 2007). Even if geochemical modeling indicates that soils on the Florida Keys and Bahamas have strong African dust component (Muhs et al., 2007) particle sizes decrease downwind as a result of more rapid gravitational settling of coarse-grained particles (van der Does et al., 2016). In addition the mineralogy and isotopic composition of dust also decreases downwind as a result of by the depletion in isotopes carried by dense minerals and the preferential settling of heavier quartz and zircon particles closer to Africa (Pourmand et al., 2014). Furthermore, van der Does et al. (2018) discussed different transport agents to explain the occurrence of large dust particles (quartz) of a few hundred microns (up to 450 µm) in Atlantic Ocean sediment traps ∼2,400 and 3,500 km away from their source in the Sahara. However, such dust particles have a much lower density (quartz = 2.65 g/cm^3) compared to zircon (4.71 g/cm^3). Although transport, turbulence, uplift in convective systems, and electrical levitation of particles have been discussed as possible explanations, a definitive reconstruction of an aeolian transport pathway has not yet been found.

In Hawaii, Vogel et al. (2021) reported apatite dust particles that range in diameter between 5 and 30 µm. Calculated trajectories showed that dust from known dust source areas in Central Asia and Northern Africa regularly reaches the Hawaiian archipelago but dust trajectories originating from the Sahara are more common than from Asian dust centers. While large and dense particles fall out faster and are thus less likely to be transported across the Pacific, even large (∼30 µm) apatite dust particles observed in Hawaii could originate from tropospheric transport. Other investigators have estimated that around 70% of dust-derived quartz in Hawaiian soils is in the range of 2–10 µm in diameter (Jackson et al., 1971).

4.1.4. Subaqueous Transport by Ocean Currents

The transport of large dense particles by ocean currents from South America to the Galápagos seems highly unlikely. The South Equatorial Current does not exceed 0.8 m/s between the mainland and the archipelago. Based on a simplified Stokes formula of Dey et al. (2019), a 100 µm zircon particle would sink at approximately 15 mm/s, meaning that it would reach a 4 km water depth after 74 hr or 213 km from the coast at a seaward flow of 0.8 m/s.

4.1.5. Far-Traveled Volcanic Pumice

Large floating pumice rafts created by eruptions of submarine volcanoes or coastal subaerial volcanoes have been reported in recent years in the western Pacific (Jutzeler et al., 2020; Ohno et al., 2022). Pumices are most abundant and most typically developed from felsic (silica-rich) igneous rocks and they have an exceedingly wide distribution over the Earth's surface. Pumice can float on water for months and is thus distributed over the sea by winds and currents until it becomes waterlogged and sinks to the bottom, where it gradually disintegrates and is incorporated in the muds and oozes of the ocean floor. In the southwest Pacific Ocean, floating pumice rafts

are driven westwards by the prevailing winds and equatorial ocean currents. This results in their accumulation mostly in eastern Australian waters or more recently in the coast of Okinawa (Ohno et al., 2022). This observation (Figure S7 in Supporting Information S1) together with a mineralogical study from 17 beaches on 11 islands (Seelos et al., 2021) hampers contamination of Galapagos beach sands by pumice rafting in the eastern Pacific.

4.1.6. Volcanic Super-Eruptions

Zircons are not very abundant in super-eruption volcanic deposits (only few % of the crystal assemblage) (Matthews et al., 2012). In addition, zircon is very dense, so only a small percentage of fine-grained crystals would travel far from the volcanoes (>1,000 km separates the Galapagos Islands from the Andean volcanic chain). That would only be a matter of concern if there were visible distal tephra of large super volcanic eruptions from elsewhere documented in Galapagos. The tephra layers described in Galapagos correspond to volcanoes in Isabela (Geist et al., 1994) and Rábida (Harpp & Geist, 2018). Reports from ultra-distal tephra deposits from super (Plinian type) eruptions (>2,000 km from Toba caldera; Indonesia and Whakamaru, >900 km from source in the Taupo Volcanic Zone; New Zealand) indicate that ash particles are fine with >70% fine particles (<63 μm) and particle size distributions with means of 64–78 and 52 μm respectively (Matthews et al., 2012). Only in proximal regions (<200 km from source) can coarser crystals be found (mean 228 μm).

In Central and South America there are ca. twenty sites (8 in Central America and 12 in the South American Andes) with a Volcanic Explosivity Index larger than 6 that generated relatively recent large explosive eruptions. Considering that stratospheric winds in South America commonly blow toward the West (https://addeyans-geography.weebly.com/global-atmospheric-circulation.html; https://earth.nullschool.net/#current/wind/surface/level/orthographic=-89.62,4.44,459/loc=-90.999,-0.182), it is interesting to note that so far tephra deposits from outside Galapagos have not been reported in the islands. On the other hand, of all volcanoes from Central and South America only Cerro Galán Caldera in Argentina has yielded rare (~540–500 Ma) zircon xenocrysts derived from basement rocks (Folkes et al., 2011).

4.1.7. Magmatic Assimilation of Detrital Oceanic Sediments

The sedimentary cover accumulated on the ocean floor since 14 Myr (age of Galapagos lithosphere) and before the volcanoes started to form is probably very thin owing to the pelagic location of the basement far from the continent and the young age of the lithosphere beneath the islands (Geist et al., 1998). Therefore, assimilation of detrital oceanic sediments accumulated below the volcanic edifices of Galápagos and on top of the pre-Galápagos mid-ocean ridge-related volcanic crust does not appear to be an important process in the evolution of magmas erupted from Galápagos volcanoes. Geist et al. (1998) indicate, based on a combination of O and He-isotopes as well as trace element data, that assimilation of oceanic crust is not an important process in the evolution of Galapagos magmas.

4.1.8. Contamination of the Asthenosphere by Subducted Material

Continental zircon grains in Galápagos lavas could indicate the presence of a component of recycled continental crust in the mantle below the islands, in line with geochemical evidence (Blichert-Toft & White, 2001; Hoernle et al., 2000), and similar to Hawai'i where old subcontinental lithospheric mantle zircon below Oahu has been recently reported (Greenough et al., 2021). The inherited zircon population in Galápagos matches, in terms of age and isotope systematics, (a) zircons from exposed basement regions of northern South America and Central America (Heilbron et al., 2017; Nadeau et al., 2013; Noguera et al., 2011), and (b) the inherited zircon grains reported from Cretaceous suprasubduction magmatic arc and mantle rocks of Cuba and Hispaniola recycled in the mantle by subduction of detritus shed from North and South America into nearby oceanic basins (Proenza et al., 2018; Rojas-Agramonte et al., 2016; Torró et al., 2018). A major Permian-Triassic age peak in the latter, corresponding to a prominent age of magmatic/metamorphic rocks in southwestern Mexico and Colombia, is also recorded in the old zircons of Galápagos. Bea et al. (2018) demonstrated that crustal zircon grains can retain their U-Pb crystallization ages even at 1,500°C, independently of how long they have remained in the mantle, if shielded in grains of Pb-free minerals. Shielding is also needed to prevent zircon from dissolving in a zircon-undersaturated basaltic liquid (Shao et al., 2019). This may help explaining the presence of continental crust zircons in the mantle, as evidence by abundant documented reports of old/xenocrystic zircon grains that survived in mantle-derived rocks from completely different geodynamic settings. These include the Pacific islands of

Hawaii (Greenough et al., 2021), and Macquarie (Portner et al., 2011), Mid-Atlantic MORB basalts and gabbros (Bea et al., 2020; Bortnikov et al., 2008, 2019; Pilot et al., 1998; Skolotnev et al., 2010), and Mauritius (Ashwal et al., 2017; Torsvik et al., 2013). Other occurrences are a variety of supra-subduction plutonic and volcanic rocks (Rojas-Agramonte et al., 2016, 2017; Smyth et al., 2007; Stern et al., 2010; Torró et al., 2018), dunites and gabbros from concentrically-zoned ultramafic bodies in the Ural Mountains of Russia (Bea et al., 2001), orogenic lherzolites such as Finero (Zanetti et al., 2016) and Ronda (González-Jiménez et al., 2017; Sánchez-Rodríguez & Gebauer, 2000).

4.1.9. Concluding Remarks

What all the above mechanisms have in common is that they cannot explain all the data at the same time. Nevertheless, in our opinion one explanation for the presence of zircon grains older than 213 Ma could be the contamination of the asthenosphere by subducted material like in Hawai'i (Greenough et al., 2021), where old xenocrystic zircons possibly reached Oahu by asthenospheric transport after subduction at Papua New Guinea. In the Galapagos' case, a likely geodynamic scenario is that detrital material carrying zircon was brought into the mantle during the West-directed Cretaceous subduction of the Central Atlantic-related Proto-Caribbean ocean beneath the Farallón plate, where the Galapagos plume was likely located (Pindell & Kennan, 2009). Horizontal upper mantle flow at relatively shallow depths (less than ~300 km) in the asthenosphere may have allowed the contaminated material to be dragged westward until it interacted with the Galápagos plume.

Based on the above arguments and considering that old exotic zircons have also been separated from basaltic and pumice samples, we can conclude that at least a portion of the old zircons found on Galapagos beaches come from the erosion of igneous rocks from islands where they have been found. However, external sources cannot be ruled out completely. Most probably the presence of old continental zircon in beaches, river deposits and caves have a multiple explanation. Further work is needed to solve this issue, including analyzing hundreds of thin sections of igneous rocks under the microscope to search for the zircon in situ and to test for its textural (inclusions), elemental (REE), structural (e.g., raman) and isotopic compositional (U-Pb/Hf/O/He) characteristics.

4.2. Galapagos Plume Array (GPA) Zircons

The most intriguing finding of our extensive zircon study is the group of GPA zircons that pre-date the Galapagos lithosphere and that have clear Hf and O isotopic mantle signatures. These are strongly similar to those of whole rocks, olivine and plagioclase from the Archipelago and associated older Carnegie, Cocos, Malpelo and Coiba ridges (Blichert-Toft & White, 2001; Geist et al., 1998; Geldmacher et al., 2003; Peterson et al., 2019; Figure 10a). Given that (a) the age of the Galápagos Islands lavas exposed to erosion is <4 Ma (Figure 10b), (b) the Galápagos lithosphere is as young as 10–14 Ma (Harpp & Geist, 2018) and (c) plate motion has moved away the pre 10–14 Ma lithosphere from above the plume head, we can conclude that any juvenile GPA zircon older than 14 Ma must have been formed and stored in the asthenosphere and have been later picked up by rising hot-spot magmas at sublithospheric depths.

Two pre-Galápagos GPA zircon grains with ages of ~18 and 22 Ma are slightly younger than the time when the Farallon plate was split by the Galapagos Spreading Center (just above the plume head) and the Cocos and Carnegie ridges began to form (23 Ma) (Wilson & Hey, 1995). The occurrence of these pre-14 Ma zircon grains implies that a fraction of the ridge-forming magmas was not fully extracted from the plume source to form oceanic crust at 18–22 Ma allowing the crystallization of zircon at depth. The same reasoning can be extended to the other GPA zircon grains older than 23 Ma. During this time, a number of magmatic events took place in the region, including the eruption of the ECCLIP with a major phase of construction at ~90 Ma (Hoernle et al., 2004). Notably, we sampled two zircon grains (93 and 94 Ma) formed close in age to this major event (Figure 10b). The GPA zircon also includes ages younger and older than the major ECCLIP event, clustering at early Tertiary (53, 55, and 65 Ma) and Jurassic (159 and two grains at 164 Ma) times (Figure 10b). The latter would allow expanding significantly back in time the magmatic history of the Galápagos plume recorded in its accreted dispersed fragments (Hoernle et al., 2004). These GPA zircon data indicate that zircon formed much earlier than the recent lavas that brought them to the surface and that it was stored at asthenospheric depths while staying unaffected by other plume-related magmatic events throughout the last ~170 Ma. This offer a unique opportunity to date the evolution of the mantle plume and to evaluate plume dynamics and asthenospheric flow.

4.3. Geodynamic Implications

A first-order observation is that our data places the minimum time of impingement of the Galapagos plume below the lithosphere to at least ~170 Ma, much earlier than commonly thought (~139–74 Ma (Dürkefälden et al., 2019; Hoernle et al., 2004; Madrigal et al., 2016; Sinton et al., 1998)). Even if most GPA zircon was sampled from surficial detritus, one of the oldest GPA zircon grains (i.e., 164 Ma) was sampled from a basaltic lava at the Alcedo Volcano on Isabela Island (Figures 2b and 3). In addition, the presence of post- and pre-14 Ma GPA (mostly the ones formed at <4 Ma) zircons in sands from almost virgin beaches and uphill streams (in the Baltra, Floreana, San Cristobal, Santa Cruz and Santa Fé islands) and inland lava tube deposits (Santa Cruz) clearly point to a local provenance from erosion of exposed volcanic rocks. Furthermore, a provenance study carried out on beaches from 11 islands of the archipelago shows that the mineral grains and rock fragments in the sand were derived from locally exposed basaltic rocks and excludes external sources (Seelos et al., 2021). All lines of evidence thus point to the crystallization of 14–164 Ma GPA zircons in the sub-lithospheric source of Galápagos lavas.

Experimental work shows that zircon can survive in the presence of mafic melt for long periods of time (millions of years) as long as the volume of melt that interacts with a zircon crystal is small or shielded within other mineral grains (Bea et al., 2018). If shielded within a Pb-free mineral, zircon grains can retain their U-Pb crystallization ages even at 1,500°C, independently of their residence time in the mantle (Bea et al., 2018; see also Bindeman et al., 2018). Shielding is also needed to prevent zircon from dissolving in a zircon-undersaturated basaltic liquid (Shao et al., 2019). Zircon grains that occur as inclusions in major mantle minerals are sealed against out-of-grain Pb loss; consequently, their U-Pb ages never reset (Bea et al., 2018). From the aforementioned we can conclude that it is possible that GPA zircon crystallized from zircon-saturated evolved basaltic liquids and remained in the plume-head regions with limited or no melt fraction for a significant period of time. Eventually, rapidly ascending magmas may pick up these zircon grains or zircon-bearing mineral or rock fragments. At this stage, dissolution of zircon occurred if exposed to the liquid and the mineral is not shielded or the magma resided long in a magma chamber. Ultimately, however, some asthenospheric zircon grains survived and reached the surface in the crystallizing magmas that, in turn, eventually reached zircon saturation and formed new zircon, as demonstrated by the overwhelming amount of young zircon grains (<4 Ma) that date Galapagos surface volcanism (Figure 10b).

Our finding of old asthenospheric mantle zircon grains challenges current ideas about asthenosphere convection and plume/lithosphere interaction (Gazel et al., 2018). Contrary to expectations, our finding implies that not all zircon was dispersed or carried away from the plume by convective flow and lithospheric motion even after more than 100 Mys residence time in the asthenosphere, which has made it possible to date the activity of the plume. Assuming that the onset of hotspot magmatism is often marked by a LIP and that the Galapagos plume is as old as ~170 Ma: where is the associated LIP of that age? Perhaps it is lost by subduction below America. In any case, but by better constraining the chronology of mantle plumes and with the help of other disciplines (e.g., geodynamics, paleomagnetism) it could be possible to predict where to find the accreted fragments of the associated LIPs and any potential ore deposits.

Finally, the results of the 2D/3D thermo-mechanical numerical simulations of plume-lithosphere interaction suggest that, once formed, some zircon crystals can remain within the asthenospheric mantle for extended periods of time. Following these results, the recorded asthenospheric zircon ages hence allow dating the Galápagos plume back to Jurassic times, a much older age than previously reported. Similar zircon observations and models of asthenospheric flow below ocean islands could apply to other plume-related hot spots. Therefore, a systematic analysis of zircon from ocean islands will allow monitoring temporal ranges of plume activity and dynamics over much longer periods than those implied by the ages of the erupted lavas, hotspot tracks, plateaus and, eventually, plume-related terranes accreted to active continental margins.

5. Conclusions

In this contribution, we show for the first time the fate of zircon grains grown in a plume environment at asthenospheric depths below the Galápagos Archipelago. Zircon grains were retrieved from basaltic and rhyolitic rocks (pumice) and sand deposits collected on the floor of a lava tube, stream beds and beaches. Our findings allow dating plume activity to at least, ~164 Ma (early Middle Jurassic). Evidence for this comes from 0 to 164 Ma

zircon with a plume isotopic signature (Galápagos Plume Array; GPA) recovered from lavas and sediments from 10 islands of the archipelago. Data from the GPA is also consistent with existing isotopic data of whole rocks, olivine and plagioclase from the Archipelago and associated Carnegie, Cocos, Malpelo and Coiba ridges. Given lithospheric plate motion, this result implies that GPA zircon predating the Galápagos lithosphere (i.e., ~14–164 Ma) formed and were stored at sublithospheric depths.

Thermo-mechanical numerical experiments of plume dynamics and plume-lithosphere interaction show a complex pattern of asthenospheric mantle flow, but they also show that old zircon grains can be stored below the archipelago within lengthy local stable asthenospheric domains (>50 Myrs in the models) to be later captured by subsequent rising plume magmas. Another important implication of our study is that by constraining the chronology of a mantle plume it will be possible to predict (with the help of other disciplines e.g., geodynamics, paleomagnetism) where to find the accreted fragments of the associated LIPs.

Data Availability Statement

Core data including analytical procedures, and tables containing zircon $\varepsilon Hf_{(t)}$ and δ18O isotopes as well as whole-rock major and trace element concentration data can be accessed through https://doi.org/10.5281/zenodo.7047729. The reference model setup for the numerical experiments can be accessed through https://doi.org/10.5281/zenodo.6967187.

References

Aarons, S. M., Aciego, S. M., & Gleason, J. D. (2013). Variable HfSrNd radiogenic isotopic compositions in a Saharan dust storm over the Atlantic: Implications for dust flux to oceans, ice sheets and the terrestrial biosphere. *Chemical Geology*, *349–350*, 18–26. https://doi.org/10.1016/j.chemgeo.2013.04.010

Akaogi, M., Hashimoto, S., & Kojitani, H. (2018). Thermodynamic properties of ZrSiO4 zircon and reidite and of cotunnite-type ZrO2 with application to high-pressure high-temperature phase relations in ZrSiO4. *Physics of the Earth and Planetary Interiors*, *281*, 1–7. https://doi.org/10.1016/j.pepi.2018.05.001

Andjić, G., Baumgartner, P. O., & Baumgartner-Mora, C. (2019). Collision of the Caribbean large igneous province with the Americas: Earliest evidence from the forearc of Costa Rica. *Bulletin of the Geological Society of America*, *131*(9–10), 1555–1580. https://doi.org/10.1130/B35037.1

Apolo, H. I., Escobar-Segovia, K., & Arcentales-Bastidas, D. (2019). Santa Cruz, Galapagos electricity sector towards a zero fossil fuel island. In *17th LACCEI international multi-conference for engineering, education, and technology: "Industry, innovation, and infrastructure for sustainable cities and communities*. 152362. https://doi.org/10.18687/LACCEI2019.1.1.170

Ashwal, L. D., Wiedenbeck, M., & Torsvik, T. H. (2017). Archaean zircons in Miocene oceanic hotspot rocks establish ancient continental crust beneath Mauritius. *Nature Communications*, *8*, 1–9. https://doi.org/10.1038/ncomms14086

Bas, M. L., Maitre, R. L., Streckeisen, A., & Zanettin, B., & IUGS Subcommission on the Systematics of Igneous Rocks. (1986). A chemical classification of volcanic rocks based on the total alkali-silica diagram. *Journal of Petrology*, *27*(3), 745–750. https://doi.org/10.1093/petrology/27.3.745

Bea, F., Bortnikov, N., Cambeses, A., Chakraborty, S., Molina, J. F., Montero, P., et al. (2022). Zircon crystallization in low-Zr mafic magmas: Possible or impossible? *Chemical Geology*, *602*, 120898. https://doi.org/10.1016/j.chemgeo.2022.120898

Bea, F., Bortnikov, N., Montero, P., Zinger, T., Sharkov, E., Silantyev, S., et al. (2020). Zircon xenocryst evidence for crustal recycling at the Mid-Atlantic Ridge. *Lithos*, *354–355*, 105361. https://doi.org/10.1016/j.lithos.2019.105361

Bea, F., Fershtater, G. B., Montero, P., Whitehouse, M., Levin, V. Y., Scarrow, J. H., et al. (2001). Recycling of continental crust into the mantle as revealed by Kytlym dunite zircons, Ural Mts, Russia. *Terra Nova*, *13*(6), 407–412. https://doi.org/10.1046/j.1365-3121.2001.00364.x

Bea, F., Montero, P., & Palma, J. F. M. (2018). Experimental evidence for the preservation of U-Pb isotope ratios in mantle-recycled crustal zircon grains. *Scientific Reports*, *8*(1), 1–10. https://doi.org/10.1038/s41598-018-30934-4

Bindeman, I. N., Schmitt, A. K., Lundstrom, C. C., & Hervig, R. L. (2018). Stability of zircon and its isotopic ratios in high-temperature fluids: Long-term (4 months) isotope exchange experiment at 850°C and 50 MPa. *Frontiers of Earth Science*, *6*. https://doi.org/10.3389/feart.2018.00059

Blichert-Toft, J., & White, W. M. (2001). Hf isotope geochemistry of the Galapagos Islands. *Geochemistry, Geophysics, Geosystems*, *2*(9). https://doi.org/10.1029/2000GC000138

Bortnikov, N. S., Sharkov, E. V., Bogatikov, O. A., Zinger, T. F., Lepekhina, E. N., Antonov, A. V., & Sergeev, S. A. (2008). Finds of young and ancient zircons in gabbroids of the Markov Deep, Mid-Atlantic Ridge, 5°54′–5°02.2′ N (Results of SHRIMP-II U-Pb Dating): Implication for deep geodynamics of modern oceans. *Doklady Earth Sciences*, *421*(1), 859–866. https://doi.org/10.1134/S1028334X08050334

Bortnikov, N. S., Silantyev, S. A., Bea, F., Montero, P., Zinger, T. F., Skolotnev, S. G., & Sharkov, E. V. (2019). U–Pb dating, oxygen and hafnium isotope ratios of zircon from rocks of oceanic core complexes at the mid-Atlantic ridge: Evidence for the interaction of contemporary and ancient crusts in the spreading center of the ocean floor. *Doklady Earth Sciences*, *489*(2), 1396–1401. https://doi.org/10.1134/S1028334X19120109

Boschman, L. M., van Hinsbergen, D. J. J., Torsvik, T. H., Spakman, W., & Pindell, J. L. (2014). Kinematic reconstruction of the Caribbean region since the early Jurassic. *Earth-Science Reviews*, *138*, 102–136. https://doi.org/10.1016/j.earscirev.2014.08.007

Burke, K., Steinberger, B., Torsvik, T. H., & Smethurst, M. A. (2008). Plume generation zones at the margins of large low shear velocity provinces on the core–mantle boundary. *Earth and Planetary Science Letters*, *265*(1), 49–60. https://doi.org/10.1016/j.epsl.2007.09.042

Cawood, P. A. (2005). Terra Australis orogen: Rodinia breakup and development of the Pacific and iapetus margins of gondwana during the neoproterozoic and paleozoic. *Earth-Science Reviews*, *69*(3), 249–279. https://doi.org/10.1016/j.earscirev.2004.09.001

Christie, D. M., Duncan, R. A., McBirney, A. R., Richards, M. A., White, W. M., Harpp, K. S., & Fox, C. G. (1992). Drowned islands downstream from the Galapagos hotspot imply extended speciation times. *Nature*, *355*(6357), 246–248. https://doi.org/10.1038/355246a0

Connolly, J. A. D. (2009). The geodynamic equation of state: What and how. *Geochemistry, Geophysics, Geosystems*, *10*(10). https://doi.org/10.1029/2009GC002540

Davies, J. H. F. L., Marzoli, A., Bertrand, H., Youbi, N., Ernesto, M., Greber, N. D., et al. (2021). Zircon petrochronology in large igneous provinces reveals upper crustal contamination processes: New U–Pb ages, Hf and O isotopes, and trace elements from the Central Atlantic magmatic province (CAMP). *Contributions to Mineralogy and Petrology*, *176*(1), 1–24. https://doi.org/10.1007/s00410-020-01765-2

Detrick, R. S., Sinton, J. M., Ito, G., Canales, J. P., Behn, M. D., Blacic, T. M., et al. (2002). Correlated geophysical, geochemical, and volcanological manifestations of plum-ridge interaction along the Galápagos Spreading Center. *Geochemistry*, *3*(10), 1–14. https://doi.org/10.1029/2002gc000350

Dey, S., Ali, S. Z., & Padhi, E. (2019). Terminal fall velocity: The legacy of Stokes from the perspective of fluvial hydraulics. *Proceedings of the Royal Society A: Mathematical, Physical & Engineering Sciences*, *475*(2228), 20190277. https://doi.org/10.1098/rspa.2019.0277

Does, M. V. D., Knippertz, P., & Zschenderlein, P. (2018). The mysterious long-range transport of giant mineral dust particles (pp. 1–8).

Downs, C. T., Bredin, I. P., & Wragg, P. D. (2019). More than eating dirt: A review of avian geophagy. *African Zoology*, *54*(1), 1–19. https://doi.org/10.1080/15627020.2019.1570335

Dürkefälden, A., Hoernle, K., Hauff, F., Wartho, J. A., van den Bogaard, P., & Werner, R. (2019). Age and geochemistry of the beata ridge: Primary formation during the main phase ($\sim$89 Ma) of the Caribbean large igneous province. *Lithos*, *328–329*, 69–87. https://doi.org/10.1016/j.lithos.2018.12.021

Ernst, R. E., & Jowitt, S. M. (2013). *Large igneous provinces (LIPs) and metallogeny* (Vol. 17, pp. 17–51). Society of Economic Geologists Special Publication.

Fisk, M., & Kelley, K. A. (2002). Probing the Pacific's oldest MORB glass: Mantle chemistry and melting conditions during the birth of the Pacific plate. *Earth and Planetary Science Letters*, *202*(3), 741–752. https://doi.org/10.1016/S0012-821X(02)00760-4

Folkes, C. B., de Silva, S. L., Schmitt, A. K., & Cas, R. A. F. (2011). A reconnaissance of U-Pb zircon ages in the Cerro Galán system, NW Argentina: Prolonged magma residence, crystal recycling, and crustal assimilation. *Journal of Volcanology and Geothermal Research*, *206*(3), 136–147. https://doi.org/10.1016/j.jvolgeores.2011.06.001

French, S. W., & Romanowicz, B. (2015). Broad plumes rooted at the base of the Earth's mantle beneath major hotspots. *Nature*, *525*(7567), 95–99. https://doi.org/10.1038/nature14876

Garnero, E. J., McNamara, A. K., & Shim, S.-H. (2016). Continent-sized anomalous zones with low seismic velocity at the base of Earth's mantle. *Nature Geoscience*, *9*(7), 481–489. https://doi.org/10.1038/ngeo2733

Gazel, E., Flores, K. E., & Carr, M. J. (2021). Architectural and tectonic control on the segmentation of the Central American volcanic arc. *Annual Review of Earth and Planetary Sciences*, *49*(1), 495–521. https://doi.org/10.1146/annurev-earth-082420-055108

Gazel, E., Trela, J., Bizimis, M., Sobolev, A., Batanova, V., Class, C., & Jicha, B. (2018). Long-lived source heterogeneities in the Galapagos mantle plume. *Geochemistry, Geophysics, Geosystems*, *19*(8), 2764–2779. https://doi.org/10.1029/2017GC007338

Geist, D., Howard, K. A., Jellinek, A. M., & Rayder, S. (1994). The volcanic history of Volcán Alcedo, galápagos archipelago: A case study of rhyolitic oceanic volcanism. *Bulletin of Volcanology*, *56*(4), 243–260. https://doi.org/10.1007/BF00302078

Geist, D., Naumann, T., & Larson, P. (1998). Evolution of Galapagos magmas: Mantle and crustal fractionation without assimilation. *Journal of Petrology*, *39*(5), 953–971. https://doi.org/10.1093/petroj/39.5.953

Geist, D. J., Snell, H., Snell, H., Goddard, C., & Kurz, M. D. (2014). A paleogeographic model of the Galápagos islands and biogeographical and evolutionary implications (pp. 145–166).

Geist, D. J., White, W. M., & McBirney, A. R. (1988). Plume-asthenosphere mixing beneath the Galapagos archipelago. *Nature*, *333*(6174), 657–660. https://doi.org/10.1038/333657a0

Geldmacher, J., Hanan, B. B., Blichert-Toft, J., Harpp, K., Hoernle, K., Hauff, F., et al. (2003). Hafnium isotopic variations in volcanic rocks from the Caribbean Large Igneous province and Galápagos hot spot tracks. *Geochemistry, Geophysics, Geosystems*, *4*(7). https://doi.org/10.1029/2002GC000477

Gibson, S. A., Geist, D. J., & Richards, M. A. (2015). Mantle plume capture, anchoring, and outflow during Galápagos plume-ridge interaction. *Geochemistry, Geophysics, Geosystems*, *16*(5), 1634–1655. https://doi.org/10.1002/2015GC005723

Gillette, D. A. (1979). Environmental factors affecting dust emission by wind erosion. In C. Morales (Ed.), *Saharan dust* (pp. 71–91). John Wiley & Sons.

González-Jiménez, J. M., Marchesi, C., Griffin, W. L., Gervilla, F., Belousova, E. A., Garrido, C. J., et al. (2017). Zircon recycling and crystallization during formation of chromite- and Ni-arsenide ores in the subcontinental lithospheric mantle (Serranía de Ronda, Spain). *Ore Geology Reviews*, *90*, 193–209. https://doi.org/10.1016/j.oregeorev.2017.02.012

Greenough, J. D., Kamo, S. L., Davis, D. W., Larson, N., Zhang, Z., Layton-Matthews, D., et al. (2021). Old subcontinental mantle zircon below Oahu. *Communications Earth & Environment*, *2*(1), 1–9. https://doi.org/10.1038/s43247-021-00261-0

Harpp, K., & Geist, D. (2002). Wolf–Darwin lineament and plume–ridge interaction in northern Galapagos. *Geochemistry, Geophysics, Geosystems*, *3*(11), 1–19. https://doi.org/10.1029/2002GC000370

Harpp, K. S. (2020). Insights into the origins and compositions of mantle plumes: A comparison of Galápagos and Hawaii. https://doi.org/10.1029/2019GC008887

Harpp, K. S., Fornari, D. J., Geist, D. J., & Kurz, M. D. (2003). Genovesa submarine ridge: A manifestation of plume-ridge interaction in the northern Galapagos islands. https://doi.org/10.1029/2003GC000531

Harpp, K. S., & Geist, D. J. (2018). The evolution of galápagos volcanoes: An alternative perspective. *Frontiers of Earth Science*, *6*, 1–16. https://doi.org/10.3389/feart.2018.00050

Harpp, K. S., Hall, P. S., & Jackson, M. G. (2014). Galápagos and easter. In *The Galápagos* (pp. 27–40). American Geophysical Union (AGU). https://doi.org/10.1002/9781118852538.ch3

Harpp, K. S., & White, W. M. (2001). Tracing a mantle plume: Isotopic and trace element variations of Galapagos seamounts (Vol. *2*).

Heilbron, M., Cordani, U. G., Alkmim, F. F. D., & Reis, H. L. S. (2017). Tectonic genealogy of a miniature continent.

Hoernle, K., Hauff, F., & van den Bogaard, P. (2004). 70 m.y. history (139–69 Ma) for the Caribbean large igneous province. *Geology*, *32*(8), 697–700. https://doi.org/10.1130/G20574.1

Hoernle, K., Werner, R., Morgan, J. P., Garbe-Schonberg, D., Bryce, J., & Mrazek, J. (2000). Existence of complex spatial zonation in the Galápagos plume for at least 14 m. *Geology*, *28*(5), 435–438. https://doi.org/10.1130/0091-7613(2000)28<435:eocszi>2.0.co;2

Holz, C., Stuut, J. W., & Henrich, R. (2004). Terrigenous sedimentation processes along the continental margin off NW Africa: Implications from grain-size analysis of seabed sediments. *Sedimentology*, *51*(5), 1145–1154. https://doi.org/10.1111/j.1365-3091.2004.00665.x

Jackson, M. L., Levelt, T. W., Syers, J. K., Rex, R. W., Clayton, R. N., Sherman, G. D., & Uehara, G. (1971). Geomorphological relationships of tropospherically derived quartz in the soils of the Hawaiian Islands. *Soil Science Society of America Journal*, *35*(4), 515–525. https://doi.org/10.2136/sssaj1971.03615995003500040051x

Jennings, E. S., & Holland, T. J. B. (2015). A simple thermodynamic model for melting of peridotite in the system NCFMASOCr. *Journal of Petrology*, *56*(5), 869–892. https://doi.org/10.1093/petrology/egv020

Jutzeler, M., Marsh, R., van Sebille, E., Mittal, T., Carey, R. J., Fauria, K. E., et al. (2020). Ongoing dispersal of the 7 August 2019 pumice raft from the Tonga arc in the southwestern Pacific ocean. *Geophysical Research Letters*, *47*(5), e1701121. https://doi.org/10.1029/2019GL086768

Kaus, B. J. P., Popov, A. A., Baumann, T. S., Püsök, A. E., Bauville, A., Fernandez, N., & Collignon, M. (2016). Forward and inverse modelling of lithospheric deformation on geological timescales. In *Presented at the NIC Symposium 2016, Schriften des Forschungszentrums Jülich* (Vol. *48*, pp. 299–307). Retrieved from http://hdl.handle.net/2128/10411

Kerr, A. C., & Mahoney, J. J. (2007). Oceanic plateaus: Problematic plumes, potential paradigms. *Chemical Geology*, *241*(3), 332–353. https://doi.org/10.1016/j.chemgeo.2007.01.019

Liu, C.-Z., Dick, H. J. B., Mitchell, R. N., Wei, W., Zhang, Z.-Y., Hofmann, A. W., et al. (2022). Archean cratonic mantle recycled at a mid-ocean ridge. *Science Advances*, *8*(22), eabn6749. https://doi.org/10.1126/sciadv.abn6749

Lonsdale, P. (2005). Creation of the Cocos and Nazca plates by fission of the Farallon plate. *Tectonophysics*, *404*(3–4), 237–264. https://doi.org/10.1016/j.tecto.2005.05.011

Madrigal, P., Gazel, E., Flores, K. E., Bizimis, M., & Jicha, B. (2016). Record of massive upwellings from the Pacific large low shear velocity province. *Nature Communications*, *7*(1), 13309. https://doi.org/10.1038/ncomms13309

Mahowald, N., Albani, S., Kok, J. F., Engelstaeder, S., Scanza, R., Ward, D. S., & Flanner, M. G. (2014). The size distribution of desert dust aerosols and its impact on the Earth system. *Aeolian Research*, *15*, 53–71. https://doi.org/10.1016/j.aeolia.2013.09.002

Matthews, N. E., Smith, V. C., Costa, A., Durant, A. J., Pyle, D. M., & Pearce, N. J. G. (2012). Ultra-distal tephra deposits from super-eruptions: Examples from Toba, Indonesia and Taupo volcanic zone, New Zealand. *Quaternary International*, *258*, 54–79. https://doi.org/10.1016/j.quaint.2011.07.010

McDonough, W. F., & Sun, S.-S. (1995). The composition of the Earth. *Chemical Evolution of the Mantle*, *120*(3), 223–253. https://doi.org/10.1016/0009-2541(94)00140-4

Meschede, M., & Barckhausen, U. (2001). The relationship of the Cocos and Carnegie ridges: Age constraints from paleogeographic reconstructions. *International Journal of Earth Sciences*, *90*(2), 386–392. https://doi.org/10.1007/s005310000155

Muhs, D. R., Budahn, J. R., Prospero, J. M., & Carey, S. N. (2007). Geochemical evidence for African dust inputs to soils of Western Atlantic islands: Barbados, the Bahamas, and Florida. *Journal of Geophysical Research*, *112*(F2), F02009. https://doi.org/10.1029/2005JF000445

Nadeau, S., Chen, W.-P., Reece, J., Lachhman, D., Ault, R., Faraco, M. T. L., et al. (2013). Guyana: The lost hadean crust of south America? *Brazilian Journal of Genetics*, *43*(4), 601–606. https://doi.org/10.5327/z2317-48892013000400002

Noguera, M. I., Wright, J., Urbani, F., & Pindell, J. (2011). U-Pb geochronology of detrital zircons from the Venezuelan passive margin: Implications for an early cretaceous proto-orinoco river system and Proto-Caribbean ocean basin paleogeography. *Geológica Acta*, *9*(3–4), 265–272. https://doi.org/10.1344/105.000001698

Nolet, G., Hello, Y., van der Lee, S., Bonnieux, S., Ruiz, M. C., Pazmino, N. A., et al. (2019). Imaging the Galápagos mantle plume with an unconventional application of floating seismometers. *Scientific Reports*, *9*(1), 1–12. https://doi.org/10.1038/s41598-018-36835-w

Ohno, Y., Iguchi, A., Ijima, M., Yasumoto, K., & Suzuki, A. (2022). Coastal ecological impacts from pumice rafts. *Scientific Reports*, *12*(1), 11187. https://doi.org/10.1038/s41598-022-14614-y

Pearce, J. A. (1996). A user's guide to basalt discrimination diagrams. In *Trace element geochemistry of volcanic rocks: Applications for massive sulphide exploration* (pp. 79–113).

Pearce, J. A. (2014). Immobile element fingerprinting of ophiolites. *Elements*, *10*(2), 101–108. https://doi.org/10.2113/gselements.10.2.101

Peterson, M. E., Wang, Z., Saal, A. E., Eiler, J. M., & Kurz, M. D. (2019). Oxygen isotope compositions of lavas from the Galapagos archipelago: Geochemical contributions from modern crustal sources. *Contributions to Mineralogy and Petrology*, *174*(2), 17. https://doi.org/10.1007/s00410-019-1550-1

Piccolo, A., Kaus, B. J. P., White, R. W., Palin, R. M., & Reuber, G. S. (2020). Plume—Lid interactions during the Archean and implications for the generation of early continental terranes. *Gondwana Research*, *88*, 150–168. https://doi.org/10.1016/j.gr.2020.06.024

Piccolo, A., Palin, R. M., Kaus, B. J. P., & White, R. W. (2019). Generation of Earth's early continents from a relatively cool Archean mantle. *Geochemistry, Geophysics, Geosystems*, *20*(4), 1679–1697. https://doi.org/10.1029/2018GC008079

Pilot, J., Werner, C.-D., Haubrich, F., & Baumann, N. (1998). Palaeozoic and proterozoic zircons from the mid-Atlantic ridge. *Nature*, *393*(6686), 676–679. https://doi.org/10.1038/31452

Pindell, J. L., & Kennan, L. (2009). Tectonic evolution of the gulf of Mexico, Caribbean and northern South America in the mantle reference frame: An update. *Geological Society, London, Special Publications*, *328*(1), 1–55. https://doi.org/10.1144/SP328.1

Portner, R. A., Murphy, M. J., & Daczko, N. R. (2011). A detrital record of lower oceanic crust exhumation within a Miocene slow-spreading ridge: Macquarie Island, Southern Ocean. *The Geological Society of America Bulletin*, *123*(1–2), 255–273. https://doi.org/10.1130/B30082.1

Pourmand, A., Prospero, J. M., & Sharifi, A. (2014). Geochemical fingerprinting of trans-Atlantic African dust based on radiogenic Sr-Nd-Hf isotopes and rare Earth element anomalies. *Geology*, *42*(8), 675–678. https://doi.org/10.1130/G35624.1

Proenza, J. A., González-Jiménez, J. M., Garcia-Casco, A., Belousova, E., Griffin, W. L., Talavera, C., et al. (2018). Cold plumes trigger contamination of oceanic mantle wedges with continental crust-derived sediments: Evidence from chromitite zircon grains of eastern Cuban ophiolites. *Geoscience Frontiers*, *9*(6), 1921–1936. https://doi.org/10.1016/j.gsf.2017.12.005

Pujol-Solà, N., Proenza, J. A., Garcia-Casco, A., González-Jiménez, J. M., Román-Alpiste, M. J., Garrido, C. J., et al. (2020). Fe-Ti-Zr metasomatism in the oceanic mantle due to extreme differentiation of tholeiitic melts (Moa-Baracoa ophiolite, Cuba). *Lithos*, *358*, 105420. https://doi.org/10.1016/j.lithos.2020.105420

Rasmussen, C., Stockli, D. F., Erickson, T. M., & Schmieder, M. (2020). Spatial U-Pb age distribution in shock-recrystallized zircon – a case study from the Rochechouart impact structure, France. *Geochimica et Cosmochimica Acta*, *273*, 313–330. https://doi.org/10.1016/j.gca.2020.01.017

Ribe, N. M., & Christensen, U. R. (1994). Three-dimensional modeling of plume-lithosphere interaction. *Journal of Geophysical Research*, *99*(B1), 669–682. https://doi.org/10.1029/93JB02386

Ribe, N. M., & Christensen, U. R. (1999). The dynamical origin of Hawaiian volcanism. *Earth and Planetary Science Letters*, *171*(4), 517–531. https://doi.org/10.1016/S0012-821X(99)00179-X

Rojas-Agramonte, Y., Garcia-Casco, A., Kemp, A., Kröner, A., Proenza, J. A., Lázaro, C., & Liu, D. (2016). Recycling and transport of continental material through the mantle wedge above subduction zones: A Caribbean example. *Earth and Planetary Science Letters*, *436*, 93–107. https://doi.org/10.1016/j.epsl.2015.11.040

Rojas-Agramonte, Y., Williams, I. S., Arculus, R., Kröner, A., García-Casco, A., Lázaro, C., et al. (2017). Ancient xenocrystic zircon in young volcanic rocks of the southern Lesser Antilles island arc. *Lithos*, *290*, 291–252. https://doi.org/10.1016/j.lithos.2017.08.002

Sánchez-Rodríguez, L., & Gebauer, D. (2000). Mesozoic formation of pyroxenites and gabbros in the Ronda area (southern Spain), followed by early miocene subduction metamorphism and emplacement into the middle crust: U–Pb sensitive high-resolution ion microprobe dating of zircon. *Tectonophysics*, *316*(1), 19–44. https://doi.org/10.1016/S0040-1951(99)00256-5

Sarnthein, M., Tetzlaff, G., Koopmann, B., Wolter, K., & Pflaumann, U. (1981). Glacial and interglacial wind regimes over the eastern subtropical Atlantic and North-west Africa. *Nature*, *293*(5829), 193–196. https://doi.org/10.1038/293193a0

Schütz, L. (1980). Long range transport of desert dust with special emphasis on the Sahara. *Annals of the New York Academy of Sciences*, *338*(1), 515–532. https://doi.org/10.1111/j.1749-6632.1980.tb17144.x

Seelos, K., Rojas-Agramonte, Y., Kröner, A., Toulkeridis, T., Inderwies, G., & Buelow, Y. (2021). Composition and provenance analysis of beach sands in an almost isolated sedimentary system—A field study of the Galápagos Archipelago. *American Journal of Science*, *321*(6), 888–906. https://doi.org/10.2475/05.2021.04

Seton, M., Müller, R. D., Zahirovic, S., Williams, S., Wright, N. M., Cannon, J., et al. (2020). A global data set of present-day oceanic crustal age and seafloor spreading parameters. *Geochemistry, Geophysics, Geosystems*, *21*(10), e2020GC009214. https://doi.org/10.1029/2020GC009214

Sevastjanova, I., Clements, B., Hall, R., Belousova, E. A., Griffin, W. L., & Pearson, N. (2011). Granitic magmatism, basement ages, and provenance indicators in the Malay Peninsula: Insights from detrital zircon U–Pb and Hf-isotope data. *Gondwana Research*, *19*(4), 1024–1039. https://doi.org/10.1016/j.gr.2010.10.010

Shao, T., Xia, Y., Ding, X., Cai, Y., & Song, M. (2019). Zircon saturation in terrestrial basaltic melts and its geological implications. *Solid Earth Sciences*, *4*(1), 27–42. https://doi.org/10.1016/j.sesci.2018.08.001

Shellnutt, J. G., Dostal, J., & Lee, T.-Y. (2021). Linking the Wrangellia flood basalts to the Galápagos hotspot. *Scientific Reports*, *11*(1), 8579. https://doi.org/10.1038/s41598-021-88098-7

Sinton, C. W., Duncan, R. A., Storey, M., Lewis, J., & Estrada, J. J. (1998). An oceanic flood basalt province within the Caribbean plate. *Earth and Planetary Science Letters*, *155*(3), 221–235. https://doi.org/10.1016/S0012-821X(97)00214-8

Skolotnev, S. G., Bel'tenev, V. E., Lepekhina, E. N., & Ipat'eva, I. S. (2010). Younger and older zircons from rocks of the oceanic lithosphere in the Central Atlantic and their geotectonic implications. *Geotectonics*, *44*(6), 462–492. https://doi.org/10.1134/S0016852110060038

Smyth, H. R., Hamilton, P. J., Hall, R., & Kinny, P. D. (2007). The deep crust beneath island arcs: Inherited zircons reveal a Gondwana continental fragment beneath East Java, Indonesia. *Earth and Planetary Science Letters*, *258*(1), 269–282. https://doi.org/10.1016/j.epsl.2007.03.044

Sobolev, S. V., Sobolev, A. V., Kuzmin, D. V., Krivolutskaya, N. A., Petrunin, A. G., Arndt, N. T., et al. (2011). Linking mantle plumes, large igneous provinces and environmental catastrophes. *Nature*, *477*(7364), 312–316. https://doi.org/10.1038/nature10385

Steinberger, B., & Torsvik, T. H. (2012). A geodynamic model of plumes from the margins of large low shear velocity provinces. *Geochemistry*, *13*(1). https://doi.org/10.1029/2011gc003808

Stern, R. J., Ali, K. A., Liégeois, J. P., Johnson, P. R., Kozdroj, W., & Kattan, F. H. (2010). °Distribution and significance of pre-Neoproterozoic zircons in juvenile Neoproterozoic igneous rocks of the Arabian-Nubian Shield. *American Journal of Science*, *310*(9), 791–811. https://doi.org/10.2475/09.2010.02

Stock, M. J., Geist, D., Neave, D. A., Gleeson, M. L. M., Bernard, B., Howard, K. A., et al. (2020). Cryptic evolved melts beneath monotonous basaltic shield volcanoes in the Galápagos Archipelago. *Nature Communications*, *11*(1), 1–13. https://doi.org/10.1038/s41467-020-17590-x

Sun, S. S., & McDonough, W. F. (1989). Chemical and isotopic systematics of oceanic basalts: Implications for mantle composition and processes. *Geological Society, London, Special Publications*, *42*(1), 313–345. https://doi.org/10.1144/gsl.sp.1989.042.01.19

Torró, L., Proenza, J. A., Rojas-Agramonte, Y., Garcia-Casco, A., Yang, J. H., & Yang, Y. H. (2018). Recycling in the subduction factory: Archaean to Permian zircons in the oceanic cretaceous Caribbean island-arc (Hispaniola). *Gondwana Research*, *54*, 23–37. https://doi.org/10.1016/j.gr.2017.09.010

Torsvik, T. H., Amundsen, H., Hartz, E. H., Corfu, F., Kusznir, N., Gaina, C., et al. (2013). A precambrian microcontinent in the Indian ocean. *Nature Geoscience*, *6*(3), 223–227. https://doi.org/10.1038/ngeo1736

Torsvik, T. H., Amundsen, H. E. F., Trønnes, R. G., Doubrovine, P. V., Gaina, C., Kusznir, N. J., et al. (2015). Continental crust beneath southeast Iceland. *Proceedings of the National Academy of Sciences of the United States of America*, *112*(15), E1818–E1827. https://doi.org/10.1073/pnas.1423099112

Torsvik, T. H., van der Voo, R., Doubrovine, P. V., Burke, K., Steinberger, B., Ashwal, L. D., et al. (2014). Deep mantle structure as a reference frame for movements in and on the Earth. *Proceedings of the National Academy of Sciences*, *111*(24), 8735–8740. https://doi.org/10.1073/pnas.1318135111

Trela, J., Vidito, C., Gazel, E., Herzberg, C., Class, C., Whalen, W., et al. (2015). Recycled crust in the galápagos plume source at 70 ma: Implications for plume evolution. *Earth and Planetary Science Letters*, *425*, 268–277. https://doi.org/10.1016/j.epsl.2015.05.036

Tsoar, H., & Pye, K. (1987). Dust transport and the question of desert loess formation. *Sedimentology*, *34*(1), 139–153. https://doi.org/10.1111/j.1365-3091.1987.tb00566.x

Valley, J. W., Lackey, J. S., Cavosie, A. J., Clechenko, C. C., Spicuzza, M. J., Basei, M. A. S., et al. (2005). 4.4 billion years of crustal maturation: Oxygen isotope ratios of magmatic zircon. *Contributions to Mineralogy and Petrology*, *150*(6), 561–580. https://doi.org/10.1007/s00410-005-0025-8

van der Does, M., Korte, L. F., Munday, C. I., Brummer, G.-J. A., & Stuut, J.-B. W. (2016). Particle size traces modern Saharan dust transport and deposition across the equatorial North Atlantic. *Atmospheric Chemistry and Physics*, *16*(21), 13697–13710. https://doi.org/10.5194/acp-16-13697-2016

Villagómez, D. R., Toomey, D. R., Geist, D. J., Hooft, E. E. E., & Solomon, S. C. (2014). Mantle flow and multistage melting beneath the Galápagos hotspot revealed by seismic imaging. *Nature Geoscience*, *7*(2), 151–156. https://doi.org/10.1038/ngeo2062

Vogel, C., Helfenstein, J., Massey, M. S., Sekine, R., Kretzschmar, R., Beiping, L., et al. (2021). Microspectroscopy reveals dust-derived apatite grains in acidic, highly-weathered Hawaiian soils. *Geoderma*, *381*, 114681. https://doi.org/10.1016/j.geoderma.2020.114681

Werner, R., Hoernle, K., van den Bogaard, P., Ranero, C., von Huene, R., & Korich, D. (1999). Drowned 14-m.y.-old Galápagos archipelago off the coast of Costa Rica: Implications for tectonic and evolutionary models. *Geology*, *27*(6), 499–502. https://doi.org/10.1130/0091-7613(1999)027<0499:DMYOGP>2.3.CO;2

White, W. M., McBirney, A. R., & Duncan, R. A. (1993). Petrology and geochemistry of the Galápagos Islands: Portrait of a pathological mantle plume. *Journal of Geophysical Research*, *98*(B11), 19533–19563. https://doi.org/10.1029/93jb02018

Wiedenfeld, D. A. (2006). Aves, the Galapagos islands, Ecuador. *Check List*, *2*(2), 1–27. https://doi.org/10.15560/2.2.1

Wilson, D. S., & Hey, R. N. (1995). History of rift propagation and magnetization intensity for the Cocos-Nazca sspreading Center. *Journal of Geophysical Research*, *100*(B6), 10041–10056. https://doi.org/10.1029/95JB00762

Zanetti, A., Giovanardi, T., Langone, A., Tiepolo, M., Wu, F. Y., Dallai, L., & Mazzucchelli, M. (2016). Origin and age of zircon-bearing chromitite layers from the Finero phlogopite peridotite (Ivrea–Verbano Zone, Western Alps) and geodynamic consequences. *Lithos*, *262*, 58–74. https://doi.org/10.1016/j.lithos.2016.06.015

References From the Supporting Information

Bodorkos, S., Stern, R. A., Kamo, S., Corfu, F., & Hickman, A. H. (2009). OG1: A natural reference material for quantifying SIMS instrumental mass fractionation of Pb isotopes during zircon dating. *AGU Fall Meeting Abstracts*, *2009*, V33B-2044.

Bouvier, A., Vervoort, J. D., & Patchett, P. J. (2008). The Lu–Hf and Sm–Nd isotopic composition of CHUR: Constraints from unequilibrated chondrites and implications for the bulk composition of terrestrial planets. *Earth and Planetary Science Letters*, *273*(1), 48–57. https://doi.org/10.1016/j.epsl.2008.06.010

Bryan, S. E., Cook, A. G., Evans, J. P., Hebden, K., Hurrey, L., Colls, P., et al. (2012). Rapid, long-distance dispersal by pumice rafting. *PLoS One*, *7*(7), e40583. https://doi.org/10.1371/journal.pone.0040583

Burov, E., Jaupart, C., & Mareschal, J. C. (1998). Large-scale crustal heterogeneities and lithospheric strength in cratons. *Earth and Planetary Science Letters*, *164*(1–2), 205–219. https://doi.org/10.1016/S0012-821X(98)00205-2

Crameri, F., Schmeling, H., Golabek, G. J., Duretz, T., Orendt, R., Buiter, S. J. H., et al. (2012). A comparison of numerical surface topography calculations in geodynamic modelling: An evaluation of the 'sticky air' method. *Geophysical Journal International*, *189*(1), 38–54. https://doi.org/10.1111/j.1365-246X.2012.05388.x

Elhlou, S., Belousova, E. A., Griffin, W. L., Pearson, N. J., & O Reilly, S. Y. (2006). Trace element and isotopic composition of GJ-red zircon standard by laser ablation. *Geochimica et Cosmochimica Acta*, *70*(18), A158. https://doi.org/10.1016/j.gca.2006.06.1383

Geist, D., Snell, H., Snell, H., Goddard, C., & Kurz, M. (2014b). *Paleogeography of the Galápagos islands and biogeographical implications*. The Galápagos: A Natural Laboratory for the Earth Sciences. Geophysical Monograph 204.

Gerdes, A., & Zeh, A. (2006). Combined U–Pb and Hf isotope LA-(MC-) ICP-MS analyses of detrital zircons: Comparison with SHRIMP and new constraints for the provenance and age of an Armorican metasediment in central Germany. *Earth and Planetary Science Letters*, *249*(1–2), 47–61. https://doi.org/10.1016/j.epsl.2006.06.039

Hirth, G., & Kohlstedt, D. L. (2003). Inside the subduction factory. Rheology of the upper mantle and the mantle wedge: A view from the experimentalists. *Geophysical Monograph Series*, *138*, 83–105.

Kröner, A., Santosh, M., & Wong, J. (2012). Zircon ages and Hf isotopic systematics reveal vestiges of Mesoproterozoic to Archean crust within the late Neoproterozoic–Cambrian high-grade terrain of southernmost India. *Advances in High-Resolution Ion-Microprobe Geochronology*, *21*(4), 876–886. https://doi.org/10.1016/j.gr.2011.05.008

Montero, P., & Bea, F. (1998). Accurate determination of 87Rb/86Sr and 147Sm/144Nd ratios by inductively-coupled-plasma mass spectrometry in isotope geoscience: An alternative to isotope dilution analysis. *Analytica Chimica Acta*, *358*(3), 227–233. https://doi.org/10.1016/s0003-2670(97)00599-0

Montero, P., Talabera, C., & Bea, F. (2017). Geochemical, isotopic, and zircon (U-Pb, O, Hf isotopes) evidence for the magmatic sources of the volcano-plutonic Ollo de Sapo Formation, Central Iberia. *Geológica Acta*, *15*(4), 245–260. https://doi.org/10.1344/GeologicaActa2017.15.4.1

Nasdala, L., Hofmeister, W., Norberg, N., Martinson, J. M., Corfu, F., Dörr, W., et al. (2008). Zircon M257 - A homogeneous natural reference material for the ion microprobe U-Pb analysis of zircon. *Geostandards and Geoanalytical Research*, *32*(3), 247–265. https://doi.org/10.1111/j.1751-908X.2008.00914.x

Popov, A. A., & Sobolev, S. V. (2008). SLIM3D: A tool for three-dimensional thermomechanical modeling of lithospheric deformation with elasto-visco-plastic rheology. *Physics of the Earth and Planetary Interiors*, *171*(1–4), 55–75. https://doi.org/10.1016/j.pepi.2008.03.007

Popov, A. A., Sobolev, S. V., & Zoback, M. D. (2012). Modeling evolution of the San Andreas Fault system in northern and central California. *Geochemistry, Geophysics, Geosystems*, *13*(8), Q08016. https://doi.org/10.1029/2012GC004086

Rudnick, R. L., & Gao, S. (2003). Composition of the continental crust. *Treatise on Geochemistry*, *3*, 659–664. https://doi.org/10.1016/B0-08-043751-6/03016-4

Rybacki, E., & Dresen, G. (2000). Dislocation and diffusion creep of synthetic anorthite aggregates. *Journal of Geophysical Research*, *105*(B11), 26017–26036. https://doi.org/10.1029/2000jb900223

Scherer, E., Münker, C., & Mezger, K. (2001). Calibration of the lutetium-hafnium clock. *Science*, *293*(5530), 683–687. https://doi.org/10.1126/science.1061372

Söderlund, U., Patchett, P. J., Vervoort, J. D., & Isachsen, C. E. (2004). The 176Lu decay constant determined by Lu–Hf and U–Pb isotope systematics of Precambrian mafic intrusions. *Earth and Planetary Science Letters*, *219*(3), 311–324. https://doi.org/10.1016/S0012-821X(04)00012-3

Vervoort, J. D., & Blichert-Toft, J. (1999). Evolution of the depleted mantle: Hf isotope evidence from juvenile rocks through time. *Geochimica et Cosmochimica Acta*, *63*(3–4), 533–556. https://doi.org/10.1016/s0016-7037(98)00274-9

Vervoort, J. D., Kemp, A. I. S., & Fisher, C. M. (2018). Hf isotope constraints on evolution of the depleted mantle and growth of continental crust. In *AGU fall meeting abstracts* (Vol. *2018*, p. V23A-07).

Williams, I. S. (1998). U-Th-Pb geochronology by ion microprobe. In *Applications of microanalytical techniques to understanding mineralizing processes* (Vol. *7*, pp. 1–32).

Wu, F.-Y., Yang, Y.-H., Xie, L.-W., Yang, J.-H., & Xu, P. (2006). Hf isotopic compositions of the standard zircons and baddeleyites used in U–Pb geochronology. *Chemical Geology*, *234*(1), 105–126. https://doi.org/10.1016/j.chemgeo.2006.05.003